Grant/Contract No. NAG5-6187

Full Proposal was submitted in response to NRA 95-OSSA-05
NASA OSSA Solar System Exploration Division
Planetary Atmospheres Program

STUDIES FOR THE LOSS OF ATOMIC AND MOLECULAR SPECIES FROM IO

Research Area:
Composition/Structure/Dynamics of Planetary Satellite Atmospheres

Final Report for the period from July 1, 1998 to June 30, 1999

Principal Investigator: Dr. Michael R. Combi

Space Physics Research Laboratory
Department of Atmospheric, Oceanic and Space Sciences
2455 Hayward Street
The University of Michigan
Ann Arbor, Michigan 48109-2143
(734) 764-7226
mcombi@umich.edu

Introduction

The general objective of this project has been to advance our theoretical understanding of Io's atmosphere and how various atomic and molecular species are lost from this atmosphere and are distributed in the circumplanetary environment of Jupiter. This grant has provided support for the activities of Dr. Michael Combi at the University of Michigan to serve as a small part in collaboration with a larger project awarded to Atmospheric & Environmental Research, Inc., with primary principal investigator Dr. William H. Smyth. Dr. Combi is the Principal Investigator and Project Manager for the Michigan grant NAG5-6187. This Michigan grant has provided for a continuation of a collaboration between Drs. Smyth and Combi in related efforts beginning in 1981, and with the object to develop and apply sophisticated theoretical models to interpret and to relate a number of new and exciting observations for the atmospheric gases of the satellite. The ability to interpret and then to relate through the theoretical fabric a number of these otherwise independent observations are a central strength of this program. This comprehensive approach provides a collective power, extracting more from the sum of the parts and seeing beyond various limitations that are inherent in any one observation. Although the approach is designed to unify, the program is divided into well-defined studies for the likely dominant atmospheric gases involving species of the SO_2 family (SO_2, SO, O_2, S and O) and for the trace atmospheric gas atomic sodium and a likely escaping molecular ion NaX^+ (where NaX is the atmospheric molecule and X represents one or more atoms).

Program of Work during the First Two Years

Work during the first two years of this program involved three major efforts. The first was adapting our model (Smyth and Combi 1991) for the extended neutral sodium corona (zenocorona or magnetonebula) for use in calculating the distribution and escape of atomic oxygen and sulfur due to the fast escape from Io from charge exchange (~50-100 km/s) with fast torus ions and direct ejection from knock-on processes (~15-50 km/s). The second was using the near sodium corona model (Smyth and Combi 1988a&b) for understanding some of the new the

eclipse and emission images of sodium by Schneider et al. (1990). We published a rather extensive paper on these results (Smyth and Combi 1997) during the first year, and a reprint of this paper is attached to this report. The third involved construction of our model for the molecular-ion source of sodium using our newly developed particle trajectory calculations for probing the physics of the nature of the molecular-ion source (Schneider et al. 1991). Our portion of this work was completed, and has already been reported in separate annual reports to NASA.

Program of Work for the Third Year

Our role in this project has been determined largely in response to the direction of Dr. Smyth at AER, Inc. who is the main Principal Investigator of the overall project. Work for this third and final year of the project involved a shift in our planned role in the program. The work, however, still falls within the specific area of studies for the loss of atomic and molecular species from Io. During the last two years Dr. Smyth and co-workers have developed a two-dimensional axisymmetric model for the detailed distribution of neutral species of the SO_2 family (namely SO_2, SO, O_2, S and O) in Io's atmosphere. The purpose of this is to provide a global picture of the distribution of atmospheric constituents from the surface, through the extended corona, and finally out to the escaping neutral gas in the circumjovian environment. More specifically, we want to put a "first-principles" physical basis to the results of our previous work (Smyth and Combi 1997) which found a particular form for the velocity distribution of atomic sodium was required to produce the observed radial (altitude) distribution of sodium in Io's corora.

In order to calculate the distribution of neutral species, it is necessary to characterize the full plasma environment including ion density, temperature and velocity. Plasma conditions are needed to characterize neutral species ionization rates and ion-neutral heating through elastic and charge exchange collisions. At his direction we supplied model results using our new three-dimensional MHD model for the interaction of Io with the corotating Jovian plasma torus, developed under a different grant (Combi et al. 1998). This included the massive set of

numerical results behind those shown in our paper, as well as comparable results from new model runs which have not yet been published. As part of this work, in addition to simply providing the model results, we have been consulting with him in their appropriate interpretation and use in the context of his neutral atmosphere model, especially as they relate to the lower boundary conditions. Because his grant year lags ours by several months, it is not yet possible to show specific results of this work here, but we expect new results in the coming months. As an example of the type of MHD results we provided, we attach a reprint of our Io MHD paper (Combi et al. 1998) published last year.

References

Combi, M.R., K. Kabin, T.I. Gombosi, D.L. DeZeeuw, K.G. Powell. Io's Plasma Environment during the Galileo Flyby: Global Three-Dimensional MHD Modeling with Adaptive Mesh Refinement. *J. Geophys. Res.* **103** (A5), 9071-9081 1998.

Schneider, N.M., J.T. Trauger, J.K. Wilson, D.I. Brown, R.W. Evans, and D.E. Shemansky, "Molecular Origin for Io's Fast Sodium," *Science* **253**, 1394-1397, 1991.

Smyth, W.H. and M.R. Combi. A General Model for Io's Neutral Gas Clouds: Mathematical Description. *Astrophys. J. Suppl.* **66**, 397-411, 1988.

Smyth, W.H. and M.R. Combi. A General Model for Io's Neutral Gas Clouds: Application to the Sodium Cloud. *Astrophys. J.* **328**, 888-918, 1988.

Smyth, W. H. and M.R. Combi, "The Sodium Zenocorona," *J. Geophys. Res.* **96**, 22711-22727, 1991.

Smyth, W. H. and M.R. Combi, "Io's Sodium Corona and Spatially Extended Cloud: A Consistent Flux Speed Distribution" *Icarus* **126**, 58-77, 1997.

ICARUS 126, 58–77 (1997)
ARTICLE NO. IS965633

Io's Sodium Corona and Spatially Extended Cloud: A Consistent Flux Speed Distribution

WILLIAM H. SMYTH

Atmospheric and Environmental Research, Inc., Cambridge, Massachusetts 02139
E-mail: smyth@aer.com

AND

MICHAEL R. COMBI

Space Physics Research Laboratory, University of Michigan, Ann Arbor, Michigan 48109

Received November 1, 1993; revised October 3, 1996

A data set composed of different groundbased observations for Io's sodium corona and spatially extended sodium cloud and covering the spatial range from Io's nominal exobase of 1.4 satellite radii to east–west distances from Io of ±100 satellite radii (R_{Io}) is used to investigate the velocity distribution of sodium at the exobase. The data set is composed of the novel 1985 eclipse measurements of Schneider *et al.* (1991, *Astrophys. J.* 368, 298–315) acquired from ~1.4 to ~10 R_{Io}, the 1985 east–west emission data of Schneider *et al.* acquired from ~4 to ~40 R_{Io}, and sodium cloud image data acquired near Io's orbital plane from ~10 to ~100 R_{Io} by a number of different observers in the 1976 to 1983 time frame. A one-dimensional east–west profile that contains Io is constructed from the data set and is analyzed using the sodium cloud model of Smyth and Combi (1988, *Astrophys. J. Supp.* 66, 397–411; 1988, *Astrophys. J.* 328, 888–918). When the directional feature in the trailing cloud is either north or south of this east–west line (i.e., not at the null condition), an isotropic modified [incomplete ($\alpha = 7/3$) collisional cascade] sputtering flux speed distribution at the satellite exobase with a peak at 0.5 km sec^{-1} provides an excellent fit to the data set for a sodium source of 1.7×10^{26} atoms sec^{-1}. In particular, the model calculation reproduces (1) the essentially symmetric column density distributions exhibited by the eclipse measurements about Io within the Lagrange sphere radius (5.85 R_{Io}, i.e., the gravitational grasp of the satellite), (2) the change in the slope of the column density observed just beyond the Lagrange sphere radius in the east–west profile of the forward cloud, but not in the trailing cloud, and (3) the distinctly different east–west brightness profiles exhibited by the forward and trailing clouds in the emission data at the more distant (~ ±20–100 R_{Io}) portions of the cloud. In contrast, the speed dispersion at the exobase for either an isotropic Maxwell–Boltzmann flux speed distribution or an isotropic classical ($\alpha = 3$) sputtering flux speed distribution (which has a higher velocity-tail population than the Maxwell–Boltzmann, but not as high as the incomplete collisional cascade sputtering distribution) is shown to be inadequate to fit the data set. To fit the enhanced trailing east–west profile observed when the directional feature is at the null condition, an additional enhanced high-speed (~15–20 km sec^{-1}) sodium population is required which is nonisotropically ejected from the satellite exobase so as to preferentially populate the trailing cloud. The need for such a nonisotropic high-speed population of sodium has also been recognized in the earlier modeling analysis of the directional features (Pilcher *et al.*, 1984, *Astrophys. J.* 287, 427–444), in the more recent lower-velocity component required in modeling the sodium zenocorona (Smyth and Combi, 1991, *J. Geophys. Res.* 96, 22711–22727; Flynn *et al.*, 1992, *Icarus* 99, 115–130), and in the very recent modeling of the directional feature reported by Wilson and Schneider (1995, *Bull. Am. Astron. Soc.* 27, 1154). A complete sodium source rate speed distribution function at Io's exobase from 0–100 km sec^{-1} is then constructed by combining the isotropic modified [incomplete ($\alpha = 7/3$) collisional cascade] sputtering flux speed distribution, the nonisotropic directional feature (lower-velocity zenocorona) source (~15–20 km sec^{-1}), and the higher-speed (~20–100 km sec^{-1}) charge-exchange source required to simulate the sodium zenocorona far from Jupiter.

1. INTRODUCTION

Atomic sodium in the Jupiter system originating from a satellite source at Io has been observed in the D_2 (5889.95 Å) and D_1 (5895.92 Å) emission lines during the past 25 yr from groundbased facilities. Using an observing slit, the sodium emission which is excited by solar resonance scattering was first discovered in 1972 by Brown (1974) very near Io, where its intensity is brightest [~many tens of kiloRaleighs (kR)] and where the sodium density is dominated by low-speed (~2 km sec^{-1} or less) ballistic atom orbits in the satellite "corona." By occultation of the

0019-1035/97 $25.00

bright region near Io, image observations (Murcray 1978; Murcray and Goody 1978; Matson *et al.* 1978) were first acquired in 1976 and 1977 for fainter (~ few to ~0.5 kR) sodium more distant from Io but still near its circular orbit (radius of 5.9 Jupiter radii) about the planet and revealed the presence of a predominant "forward cloud" and a less spatially extensive "trailing cloud" that moved with the satellite. This sodium has been characterized primarily by a source of low-speed (~2.6–4 km sec^{-1}) atoms that have sufficient energy to just escape from Io with an excess velocity of only ~1 km sec^{-1} (or so) and thereby remain gravitationally bound to Jupiter fairly near the satellite orbit. Additional observations (Pilcher *et al.* 1984; Goldberg *et al.* 1984) of even fainter (~1 to 0.2 kR) sodium in the early 1980's revealed a "directional feature" attached to Io in the trailing cloud that oscillated north and south about the satellite plane with a phase and period determined by the Io System III longitude angle. This sodium source was characterized by atoms with speeds ~20 km sec^{-1} ejected nonisotropically from the satellite so as to populate the trailing cloud and the circumplanetary space at larger radial distances beyond Io's orbit. From earlier slit measurements in 1974 (Trafton and Macy 1978), fainter (~30 R) sodium emissions well beyond Io's orbit had been observed at a radial distance of ~60 planetary radii, while from more recent images (Mendillo *et al.* 1990), very faint (~1 R) sodium emissions were observed at radial distances of ~400–500 planetary radii. Sodium at these larger radial distances is called the "magneto-nebula" or "sodium zenocorona" and is thought to be populated primarily by a nonisotropic charge-exchange source of high speed (~15–100 km sec^{-1}) atoms at Io with velocity skewed in the forward direction of corotational plasma motion past the satellite, and secondarily by a narrow forward sodium jet produced by a spatially distributed molecular ion source (Wilson and Schneider 1994). Most of this sodium escapes the Jupiter system, forms a sodium pause in the sunward direction at ~2300 planetary radii because of solar radiation acceleration, and is eventually lost to the solar wind by photoionization (Smyth and Combi 1991).

The observations of sodium emissions on many different spatial scales in the Jupiter system thus indicate that its atomic source at Io's exobase must have a wide dispersion of speeds. Modeling of these observations has in the past been mostly undertaken separately for only one of these spatial regions at a time. Although the higher velocity dispersions for the sodium zenocorona may be reasonably well understood because of its large spatial structure and the lack of any significant sodium lifetime impact of the magnetosphere, a consistent source for the slower sodium in Io's corona and in the forward and trailing clouds near its orbit has not been established. The recent determination of the sodium spatial profile in the Io corona obtained from the groundbased eclipse data of Schneider (1988; Schneider *et al.* 1987, 1991) coupled with earlier emission observations, however, now provides a viable observational base from which it is possible to pursue the nature of this slower sodium. The investigation of a consistent exobase sodium source for Io's corona and the forward and trailing clouds near its orbit is therefore undertaken in this paper. A consistent flux speed distribution at the exobase is determined, and the corresponding sky-plane spatial distribution of sodium near Io is presented. Sodium source information obtained from previous modeling analysis of Io's corona and the forward and trailing clouds is first summarized in Section 2. The observational data base to be investigated in this paper is presented in Section 3. Modeling of an east–west spatial profile determined from this observational data base is undertaken in Section 4. Discussion and conclusions are presented in Section 5.

2. EARLIER SODIUM MODELING

The major modeling analysis studies for the spatial distribution of sodium near Io and its orbit are summarized in Table I. The summary is divided into three observed spatial regions: (1) the Io corona located within the satellite Lagrange sphere (average radius of 5.81 R_{Io} or ~3 arcsec), (2) the neutral cloud located beyond the Lagrange sphere and near Io's orbit, and (3) the north–south oscillating directional feature, observed to trail Io in its orbit. Modeling analysis studies for the Io corona are further subdivided into early observations of the average intensity in an 8 × 3 arcsec slit centered on Io reported by Bergstralh *et al.* (1975, 1977) that indicated an east–west intensity asymmetry of ~1.25 and later observations for one-dimensional column density profiles within the Lagrange sphere reported by Schneider *et al.* (1987, 1991).

2.1. Corona: East–West Intensity Asymmetry

In Table I, the early studies of Smyth (1983) for sodium atoms ejected monoenergetically from Io's exobase established that small scale structures in the D-line intensity profile observed as a function of the Io geocentric phase angle (Bergstralh *et al.* 1975, 1977) could arise from modulation of the atoms' escape rate from Io caused by the action of solar radiation acceleration in the D-lines. These modulations occur primarily for exobase speeds near 2.0 and 2.1 km sec^{-1}, which are near the escape-speed threshold of the Lagrange sphere. Later studies of Smyth and Combi (1987a) showed that the main reason for the east–west intensity asymmetry was, however, an east–west electric field which altered the plasma properties at Io's orbit so as to increase the sodium lifetime and hence sodium abundance when Io was preferentially east of Jupiter. More complex modeling studies of Smyth and Combi (1988b) constrained the flux velocity dispersion for sodium at Io's exobase by simultaneously fitting the average east–west

TABLE I
Summary of Modeling Studies for the Spatial Distribution of Sodium Near Io and Its Orbit

		Sodium Source								Sodium Lifetime		Orbital Dynamics			
		Mono-energetic Atom Ejection	Maxwell-Boltzman Flux Distribution		Cascade Flux Speed Distribution										
Spatial Region	Topic Studied	Speed (km s^{-1})	T (K)	V_{peak} (km s^{-1})	α	V_b (km s^{-1})	V_{peak} (km s^{-1})	V_{max} (km s^{-1})	Angular Nature[a]	Plasma Torus Description	Lifetime (hrs)	Io's Mass Included	Jupiter's Mass Included	Radiation Pressure Included	Reference
I. Corona	e-w intensity asymmetry[b]	2.0-2.6	-	-	-	-	-	-	isotropic	cut-off	20	yes	yes	yes	Smyth 1983
	e-w intensity asymmetry[b]	2.6	-	-	-	-	-	-	isotropic	2-D	variable	yes	yes	yes	Smyth and Combi 1987a
	e-w intensity asymmetry[b]	-	460; 12,300	0.71; 3.65	7/3	<0.4; 2.2	<0.5; 2.9	46.6	band, isotropic	2-D	variable	yes	yes	yes	Smyth and Combi 1988b
	column-density profile[c]	2.6	-	-	-	-	-	-	isotropic	2-D	varialbe	yes	yes	yes	Smyth and Combi 1987b,c
	column-density profile[c]	-	-	-	3	0[d]	-	∞	isotropic	cut-off	3, ∞	yes	no	no	McGrath 1988
	column-density profile[c]	-	1000	1.04	-	-	-	-	isotropic	uniform	∞	yes	no	no	Summers et al. 1989
	column-density profile[c]	3.0	-	-	-	-	-	-	isotropic	uniform	?	yes	no	no	Ip 1990
	column-density profile[c]	-	1500	1.28	-	-	-	-	isotropic	uniform	∞	yes	no	no	Schneider et al. 1991
II. Cloud	general spatial nature	3.5	-	-	-	-	-	-	isotropic	uniform	30, 47	yes	yes	no	Carlson et al. 1975
	general spatial nature	-	5000	2.3	-	-	-	-	isotropic	long-lived limit	-	no	yes	no	Fang et al. 1976
	evolution and 2-D nature	2, 3	-	-	-		-	-	isotropic	cut-off	50	yes	yes	no	Smyth and McElroy 1977
	1-D brightness morphology[f]	-	-	-	3	4	4	∞	I-L hemisphere[g]	uniform	28	yes	yes	no	Matson et al. 1978
	2-D brightness morphology[h]	2.6, 3	-	-	-	-	-	-	I, I-T hemisphere[i]	cut-off	15, 20	yes	yes	no	Smyth and McElroy 1978
	e-w orbital asymmetry[j]	2.6	-	-	-	-	-	-	I T hemisphere[i]	cut-off	20	yes	yes	yes	Smyth 1979
	radial and vertical structure	(3,5,7,9,11,13)[k]	-	-	-	-	-	-	I hemisphere	uniform	56	no	yes	no	Macy and Trafton 1980
	1-D brightness morphology	-	-	-	3[l]	4[l]	4[l]	∞ [l]	I-L hemisphere[l]	1-D	variable	yes	yes	no	Goldberg et al. 1980
	e-w orbital asymmetry	2.6	-	-	-	-	-	-	I hemisphere	cut-off	20	yes	yes	yes	Smyth 1983
	2-D brightness morphology	2.6	-	-	-	-	-	-	band, isotropic	2-D	variable	yes	yes	yes	Smyth and Combi 1988b
III. Directional Feature	spacetime structure[m]	~20	-	-	-	-	-	-	O, ~$\perp$ to Io's motion	2-D	variable	yes	yes	yes	Pilcher et al. 1984
	collision cross sections	-	-	-	3	0[n]	-	-	~$\perp$ to Io's motion	-	-	-	-	-	Sieveka and Johnson 1984
	nearer zenocorona structure	-	-	~20± 12[p]	-	-	-	-	tangential ± isotropic	photoionization	~400 hr	no	no; Sun yes	yes	Smyth and Combi 1991
	nearer zenocorona structure	-	-	~20± 12[p]	-	-	-	-	tangential ± isotropic	photoionization	~400 hr	no	yes	no	Flynn et al. 1992
	spacetime structure	-	-	20± 10-20[q]	-	-	-	-	tangential ± isotropic	none	∞	no	yes	no	Wilson and Schneider 1995

[a] regarding Io's exobase; L=leading, I=inner, T=trailing, O=outer

[b] east-west intensity asymmetry data of Bergstralh et al. (1975, 1977)

[c] early (i.e., partial) Na eclipse data set from Schneider et al. (1987).

[d] used cut-off energy: $E_{min} \leq E < \infty$; $E_{min} = k T_{exobase}$; $T_{exobase}$=1500 K (i.e. a 1.04 km s^{-1} cut-off speed).

[e] complete eclipse data set from Schneider (1988) and Schneider et al. (1991).

[f] two sodium cloud images of Matson et al. (1978).

[g] I-L hemisphere centered 30° longitude (0° longitude facing Jupiter, 90° longitude is the leading point in the orbit).

[h] fifty-six sodium cloud images of Murcray (1978) and Murcray and Goody (1978).

[i] I-T hemisphere centered on -40° longitude.

[j] east-west orbital asymmetry data of Goldberg et al. (1978).

[k] velocity components equally weighted.

[l] distribution parameters from Carlson (1995, private communication); I-L hemisphere centered on 45° longitude.

[m] from images of Pilcher et al. (1984).

[n] used cut-off energy of 0.5 ev (i.e., Na cut-off speed of 2.0 km s^{-1}).

[p] tangential speed to Io's orbit at Io position ± most probable speed of an isotropic Maxwell-Boltzmann.

[q] tangential speed to Io's orbit at Io position ± most probable speed of an isotropic Gaussian.

intensity asymmetry and also the general spatial morphology of the forward sodium cloud, located on a much larger spatial scale well beyond the Lagrange sphere. These studies showed that the sodium ejection speed at the exobase required to fit the east–west intensity asymmetry is double-valued, having a lower value of ≤ 1 km sec^{-1} and a higher value in the range 2.6–3.65 km sec^{-1}. For a Maxwell–Boltzmann flux distribution, the lower and higher most probable speed values were 0.71 km sec^{-1} (T = 460 K) and 3.65 km sec^{-1} (T = 12,300 K). Neither distribution was, however, suitable for properly populating the forward cloud. The lower value produces essentially only ballistic atom orbits which could not populate the forward cloud, while the higher value was significantly larger than the nominal ~2.6 km sec^{-1} characteristic monoenergetic velocity required to reproduce the proper spatial morphology of the forward cloud as a function of the Io geocentric phase angle. For a Maxwell–Boltzmann flux distribution with a more nominal thermal exobase temperature in the range ~1000–2000 K, the calculated east–west intensity ratio was much higher than the observed value, with the atoms still contributing primarily to the corona density and again far too deficient in energy to contribute any significant sodium to the forward cloud. For the preferred (α = 7/3) modified-sputtering distribution of Smyth and Combi (1988b) with source strength ~2×10^{26} atoms sec^{-1}, the lower and higher speed values were $\leq$0.5 and ~2.9 km sec^{-1}, respectively, with the latter value being preferred because of its closer proximity to the ~2.6 km sec^{-1} characteristic velocity for the forward cloud. Interestingly, however, it is actually the lower value that will be shown in this paper to reproduce the correct spatial profile for sodium both within the Lagrange sphere and beyond in the more distant neutral cloud.

2.2. *Corona: Column Density Profile*

In Table I, modeling studies of Smyth and Combi (1987b,c) determined that typical forward cloud brightness data for the sodium cloud could be properly simulated well beyond the Lagrange sphere radius of ~5.81 R_{Io} by a sodium source of ~1×10^{26} atoms sec^{-1} ejected monoenergetically from Io's exobase with a characteristic velocity of ~2.6 km sec^{-1}. They also established that this same sodium source reproduced the column density profile of Schneider *et al.* (1987) within the Lagrange sphere down to a radius of ~3.5 R_{Io}. For a radius smaller than ~3.5 R_{Io}, the calculated profile was lower than the observed profile, indicating that lower (ballistic) velocity components are required, in addition, as part of a more realistic flux velocity dispersion. A similar behavior for the simulated column density profile, with an even more dramatic departure from the observed profile both inside and outside the Lagrange sphere, was also later shown by a model calculation of Ip (1990), who assumed an exobase speed of 3 km sec^{-1} but did not include the gravity of Jupiter so as to properly include the near zero escape speed conditions for sodium at the Lagrange sphere. Adopting for sodium atoms at the exobase a simple (i.e., binding-energy velocity v_b = 0) classical sputtering energy distribution with a low energy cut-off and also excluding Jupiter's gravity, McGrath (1988) modeled the column density within the Lagrange sphere and produced a profile with a slope slightly less steep than the observation for an infinite sodium lifetime and a slope somewhat steeper than the observation for a sodium lifetime of 3 hr. Alternatively adopting a Maxwell–Boltzmann flux distribution, assuming an infinite sodium lifetime, and similarly excluding Jupiter's gravity, Summers *et al.* (1989) and Schneider *et al.* (1991) modeled the column density within the Lagrange sphere region and produced a profile that reasonably well matched the observed profile for an exobase temperature, respectively, of 1000 K based on the partial eclipse data set (Schneider *et al.* 1987) and of 1500 K based on the complete eclipse data set (Schneider *et al.* 1991). Although these different flux velocity distributions reasonably fit the observations within the Lagrange sphere, it is clear from the earlier studies of Smyth and Combi (1988b) that these Maxwell–Boltzmann distributions are energetically deficient and inappropriate for populating the neutral cloud and, furthermore, that the more energetically promising sputtering distribution cannot be investigated adequately near or beyond the Lagrange sphere radius without properly including the gravity of Jupiter, solar radiation acceleration, and the spacetime variable sodium lifetime in the plasma torus. This study will be undertaken in Section 4.

2.3. *Sodium Cloud*

The early studies in Table I for the sodium cloud were general in nature, probing its poorly documented spatial and angular extent about the planet. Based upon the solar resonance scattering excitation mechanism for sodium (Bergstralh *et al.* 1975) and limited angular extent data determined by slit-averaged intensity data, Carlson *et al.* (1975) undertook monoenergetic (3.5 km sec^{-1}) model calculations and estimated that the sodium cloud lifetime (assumed to be spatially uniform) was likely determined by electron impact ionization by the (then very poorly characterized) plasma in the planetary magnetosphere. This general picture for the cloud was confirmed by more extensive model calculations performed by Fang *et al.* (1976) and Smyth and McElroy (1977), the latter of which explored the time evolution and two-dimensional nature of the cloud for exobase velocities near the Io Lagrange escape speed. The acquisition of sodium cloud images in late 1976 and early 1977 brought this subject into dramatic focus. For a classical sputtering flux distribution that peaked at 4 km sec^{-1}, Matson *et al.* (1978) successfully

modeled a one-dimensional east–west brightness profile (derived from a cloud image) which extended from Io in the forward cloud to ~80 R_{Io} and in the trailing cloud to ~40 R_{Io} but which excluded sodium emission within Io's corona. The analysis (Smyth and McElroy 1978) of a much larger sodium cloud image data set (Murcray 1978) also indicated that the forward cloud could be characterized by an exobase ejection speed of ~2.6 km sec^{-1} and that its changing intensity pattern could be understood as the changing viewing perspective of an approximately steady state cloud on the sky plane as Io moved on its orbit around Jupiter. The observed predominance of the forward sodium cloud over the trailing cloud was accomplished in all these models by limiting the exobase source area to a hemisphere (see Table I) and by limiting the assumed spatially uniform lifetime so as to dynamically select sodium atom orbits that would primarily populate the forward cloud. Additional modeling studies by Macy and Trafton (1980) of the radial and vertical cloud structure on a larger spatial scale indicated source dispersion speeds at least up to 13 km sec^{-1} were, however, required to explain a variety of other observations. Additional model studies (Smyth 1979, 1983) showed that the newly discovered east–west orbital asymmetry of the sodium cloud (Goldberg *et al.* 1978) was not source related but was due to the perturbing action of solar radiation acceleration on the sodium atom orbits. Adopting a one-dimensional radially dependent sodium lifetime in the plasma torus based upon limited Voyager spacecraft data and an asymmetric exobase source for a classical sputtering distribution with a peak velocity at 4 km sec^{-1}, Goldberg *et al.* (1980) successfully modeled a one-dimensional east–west brightness profile acquired during the Voyager 1 encounter for distances extending from Io in the forward cloud to ~80 R_{Io} and in the trailing cloud to ~30 R_{Io}. Later modeling by Smyth and Combi (1988b) using a more accurate two-dimensional space- and time-dependent sodium lifetime in the plasma torus and an isotropic (or near isotropic) exobase sodium source of ~2 × 10^{26} atoms sec^{-1} demonstrated that the predominant forward cloud was caused by the highly radially dependent sink for sodium in the plasma torus and not by a nonisotropic source. The deduced characteristic or most probable exobase speed for the more definitive modeling of the forward sodium cloud above is, therefore, in the range ~2.6 to 4 km sec^{-1} and is much larger than required to characterize the sodium column density profile in Io's corona. A new flux speed distribution is therefore needed for consistency and is determined in Section 4.

2.4. *Directional Feature*

In Table I, observations acquired in 1980 and 1981 by Pilcher *et al.* (1984) for weaker D-line emissions in the trailing portion of the sodium cloud allowed them to discover an elongated feature in the brightness distribution that on the sky plane was directed away from Jupiter and was inclined sometimes to the north and sometimes to the south of the satellite's orbital plane. The north–south direction of the feature was shown to be correlated with Io's magnetic longitude and suggested a formation mechanism involving the oscillating plasma torus. Modeling analysis by Pilcher *et al.* indicated that the feature resulted from a high-velocity (~20 km sec^{-1}) sodium source that was at near right angles to Io's orbital motion with a source strength required on the outer satellite hemisphere of ~1 × 10^{26} atoms sec^{-1}. This peculiar directionality of the source was investigated by Sieveka and Johnson (1984), who concluded that it was likely produced by direct collisional ejection of neutral sodium from the exosphere by the corotating plasma flow past Io. Modeling of the sodium zenocorona (Smyth and Combi 1991; Flynn *et al.* 1992) showed that it was consistent with a two-component exobase source: a similar high-velocity (~20 km sec^{-1}) sodium source of ~1 × 10^{26} atoms sec^{-1} for the spatial distribution nearer the planet and an even higher-velocity (~57 km sec^{-1}) sodium source of ~2 × 10^{26} atoms sec^{-1} for the spatial distribution further from the planet. Both source components, however, were based on ion–neutral charge exchange processes in Io's exosphere and were hence composed of a speed tangential to Io's orbit at Io's position plus an isotropic Maxwell–Boltzmann distribution with a most probable speed of about one-third of the tangential speed in the Jupiter frame (i.e., one-third of ~37 and ~74 km sec^{-1}, respectively). In Table I, the lower component is therefore symbolically denoted in the Io frame by 20±12 km sec^{-1}. Recent modeling of the directional features has also been reported by Wilson and Schneider (1995), who used a similar lower component source denoted in Table I by 20 ± 10–20 km sec^{-1}, where the isotropic portion of their source may be variable in magnitude. A spatially distributed molecular-ion source has also been used to model the sodium zenocorona (Flynn 1993), but appears to be of secondary importance due to its smaller source rate and erratic presence.

3. OBSERVATIONAL DATA BASE FOR MODELING

To describe the entire spatial distribution of sodium in Io's corona and beyond in the extended neutral clouds, three different types of sodium observations obtained on very different spatial scales are combined. For Iocentric distances, the combined data set is composed of the novel 1985 eclipse measurements of Schneider *et al.* (1991) acquired from ~1.4 to ~10 R_{Io}, the 1985 east–west emission data of Schneider *et al.* (1991) acquired from ~4 to ~40 R_{Io}, and sodium cloud image data acquired near Io's orbital plane from ~10 to ~100 R_{Io} by a number of different

TABLE II
Io Eclipse and Emission Observations for 1985

Date	UT Midpoint	Io Geocentric Phase Angle Range (deg)	Io System III Longitude Range (deg)	Spectrum ID	Type of Observation		Dominant Spatial Profile	Directional Feature Orientation	Enhance Doppler Signature	D_2 Emission Profile Power Law Fit [f] Exponent		Amplitude (kR)	
					Eclipse	Emission				East Profile	West Profile	East Profile	West Profile
August 27	0714	61.4 ± 0.7	29.9 ± 2.3	85g188		1	forward	null	trailing/forward	1.67 (F)	1.57 (T)	191	124
	0720	62.3 ± 11.0	32.9 ± 35.8	a	1		---	---	---				
	0830	72.2 ± 1.1	65.1 ± 3.4	85g196		2	symmetric	south	no	1.85 (S)	1.80 (S)	169	142
September 13	0641	276.6 ± 0.7	194.7 ± 2.3	85h032		3	trailing	null/north	trailing	---	---	---	---
September 14	0245	87.7 ± 0.7	31.4 ± 2.3	85h102		4	trailing	null	trailing	1.23 (S/T)	1.80 (S/F)	89	188
	0326	93.5 ± 4.2	50.5 ± 13.7	b	2		---	---	---				
	0416	100.6 ± 0.4	73.6 ± 1.4	85h113		5	g	south	no	1.27 (T)	---	66	---
September 15	0316	294.7 ± 0.7	353.7 ± 3.0	85h152		6	trailing	null	trailing	---	---	---	---
	0500	309.4 ± 11.5	41.7 ± 37.4	c	3		---	---	---				
September 21	0604	100.5 ± 1.6	112.5 ± 5.2	d	4		---	---	---				
September 23	0230	117.2 ± 0.7	267.6 ± 2.3	85h433		7	forward	north	no	2.05 (T)	1.57 (F)	342	135
	0301	121.6 ± 0.4	281.9 ± 1.2	85h436		8	forward	north	no	1.96 (T)	1.54 (F)	283	138
	0356	129.3 ± 2.0	307.3 ± 6.7	e	5		---	---	---				
	0534	143.1 ± 0.7	352.9 ± 2.3	85h457		9	forward	null	no	2.16 (T)	1.64 (F)	374	165

a. Eclipse 1 : 85g179, 85g181, 85g185, 85g188, 85g192, 85g193, 85g196

b. Eclipse 2 : 85h103, 85h104, 85h105, 85h106, 85h107, 85h108, 85h109, 85h110, 85h112

c. Eclipse 3 : 85h153, 85h154, 85h155, 85h157, 85h159, 85h162, 85h163

d. Eclipse 4 : 85h287, 85h288, 85h289, 85h290, 85h291 85h292, 85h293, 85h294, 85h295

e. Eclipse 5 : 85h441, 85h442, 85h443, 85h444, 85h445, 85h446, 85h447, 85h448, 85h449, 85h450

f. Profile points inside of 4 R_{Io} are excluded; power law fit $A\ r^{-\beta}$, where A is the amplitude, β is the exponent, and r is in units of R_{Io}; F = forward cloud; S = symmetric turning point; T = trailing cloud.

g. Not sufficient data west of Io to compare spatial profils (see Table III).

(Note one lower-bound data point from eclipse 4 at a distance from the center of Io of 1.17 R_{Io} is excluded in the analysis since it is well within the nominal exobase radius of 1.4 R_{Io})

observers in the 1976 to 1983 time frame. For modeling purposes in Section 4, a one-dimensional east–west profile centered on Io is constructed from this data set. From the data of Schneider *et al.* (1991), five higher quality eclipse profiles and nine higher quality emission profiles have been selected, and their observational dates, times, Io angular parameters, spectral ID numbers, and the numbering of these interleaved observations as adopted in this paper are summarized in Table II. The D_2 brightnesses for the emission profiles in Table II, previously published only in a graphical format, are given numerically in Table III as provided by Schneider (1990, 1995, both private communications). For the sodium cloud data, fourteen images in the D_2 emission line acquired in the 1976–1983 time interval (Murcray 1978; Murcray and Goody 1978; Matson *et al.* 1978; Goldberg *et al.* 1980, 1984; Morgan 1984, private communication) have been selected, with values for the east–west D_2 brightness profiles of the forward and trailing clouds extracted and summarized in Table IV.

The eclipse observations provide the most accurate information in the radial interval from ~1.4 to 6 R_{Io} for the atomic sodium column density profile in the corona within the Lagrange sphere of Io (i.e., a radius of 5.81 R_{Io}) and yield an essentially symmetric column density profile about Io with a power law fit $N\ (1.4 \leq r \leq 5.85) = 2.55 \times 10^{12} r^{-2.48}$, where N is in units of atoms cm^{-2} and r is the distance from the Io's center in units of R_{Io}. This power law fit, however, undercuts the eclipse data beyond the Lagrange radius, and this reduced slope will later be seen to be caused by the dominant planetary gravitational field beyond Io's Lagrange radius. The emission observations provide accurate information for the sodium D_2 brightness from just within the Lagrange sphere outward into the nearer portion of the sodium cloud (i.e., ~4–40 R_{Io} from Io's center) with a power law fit $I_{D_2}(r \geq 4) = 101\ r^{-1.45}$, where I_{D_2} is in units of kiloRayleighs (kR) and where the D_2 brightness of ~100 kR as r approaches Io's surface is consistent (see Brown and Yung 1976) with the maximum sodium column density of $\sim 1 \times 10^{12}$ atoms cm^{-2} deduced from the eclipse data. The brightnesses for the different observed profiles in Table III, however, vary by a factor of ~3 to almost 5 at the same distance from Io but have error bars that are no larger than ±30%, suggesting that the large variation is real and likely correlated with Io geocentric phase angle, Io System III longitude, and the east–west asymmetry in the plasma torus, as is the case for sodium cloud image data. The closer spatial regions covered by the eclipse data and the near Io emission data are, however, masked in the cloud images by a circular (or nearly circular) occulting mask of ~10 R_{Io} in radius centered on Io. The sodium cloud image data in Table IV, as illustrated in Fig. 1, hence contribute to the east–west brightness profiles for Iocentric distances from ~10 to ~100 R_{Io}.

The structure of the sodium cloud emission brightness on the sky plane has been historically divided into a forward cloud, so-called because it appears ahead of the satellite in its orbit (i.e., in Fig. 1 located right (west) of Io in image A and left (east) of Io in images B and C), and a corresponding trailing cloud that appears behind the

TABLE III
Emission Data for 1985

	Radial Distance From Io (satellite radii)	D_2 Intensity‡(kR) Emission 1 61.4° 27 August (85g188)	Emission 2 72.2° 27 August (85g196)	Emission 4 87.7° 14 September (85h102)	Emission 5 100.6° 14 September (85h113)	Emission 7 117.2° 23 September (85h433)	Emission 8 121.6° 23 September (85h436)	Emission 9 143.1° 23 September (85h457)	Emission 3* 276.6° 13 September (85h032)	Emission 6 294.7° 15 September (85h152)
	-29.92					0.69 ± 0.17	0.93 ± 0.18	0.66 ± 0.16		
	-29.65									1.12 ± 0.19
	-24.48								1.40 ± 0.21	
	-21.76					1.19 ± 0.19	0.84 ± 0.17	0.95 ± 0.18		
	-16.32					1.38 ± 0.20	2.10 ± 0.26		2.22 ± 0.27	
	-15.78							1.74 ± 0.23		2.15 ± 0.26
	-14.96				1.91 ± 0.24					
	-10.88	3.16 ± 0.35				2.90 ± 0.33	3.29 ± 0.36	3.38 ± 0.37	4.40 ± 0.46	
↑	-9.52			3.17 ± 0.35						
West	-6.80	5.21 ± 0.54	4.50 ± 0.47	6.41 ± 0.66		7.49 ± 0.76	7.76 ± 0.79		11.54 ± 1.16	
	-4.08	14.65 ± 1.47	11.29 ± 1.14	14.71 ± 1.48				7.54 ± 0.77	28.69 ± 2.87	
	-3.81									18.75 ± 2.63
	-2.18	24.31 ± 3.40	18.39 ± 2.57	24.12 ± 3.38		25.61 ± 3.59	25.01 ± 3.50	21.00 ± 2.94	45.47 ± 6.37	
	-1.09	27.46 ± 3.84	19.99 ± 2.80	27.14 ± 3.80		29.95 ± 4.19	28.72 ± 4.02	23.89 ± 3.34	48.61 ± 6.81	
	-0.82									24.85 ± 3.48
Io	0.00	27.44 ± 3.84	19.19 ± 2.69	27.14 ± 3.80		27.90 ± 3.91	30.16 ± 4.22	23.97 ± 3.36	45.56 ± 6.38	
	0.27									25.27 ± 3.54
	1.09	25.87 ± 3.62	19.35 ± 2.71	26.65 ± 3.73	23.03 ± 3.22	26.31 ± 3.68	26.39 ± 3.69	22.84 ± 3.20	39.45 ± 5.52	
	1.36									22.90 ± 3.21
	2.18	25.19 ± 3.53	16.87 ± 2.36	25.68 ± 3.60	19.60 ± 2.74	22.42 ± 3.14	23.91 ± 3.35	20.21 ± 2.83	33.60 ± 4.70	
	3.26									11.53 ± 1.61
	4.08	17.60 ± 1.77	11.92 ± 1.20	18.10 ± 1.82	11.87 ± 1.20	15.54 ± 1.56	14.83 ± 1.49	12.52 ± 1.26	20.06 ± 2.01	
	5.98									4.79 ± 0.50
East	6.80	8.31 ± 0.84	5.52 ± 0.57	8.17 ± 0.83	5.52 ± 0.57	7.09 ± 0.72	7.10 ± 0.73	6.02 ± 0.62	7.52 ± 0.77	
↓	10.06									1.66 ± 0.22
	10.88	3.40 ± 0.37	1.94 ± 0.25	3.84 ± 0.41	3.21 ± 0.35	2.47 ± 0.29	2.47 ± 0.29	2.26 ± 0.27	2.73 ± 0.31	
	15.50									0.77 ± 0.17
	16.32			2.84 ± 0.32	1.81 ± 0.24	1.03 ± 0.18	1.11 ± 0.19	0.82 ± 0.17	1.39 ± 0.20	
	21.76			2.25 ± 0.27		0.68 ± 0.16	0.75 ± 0.17	0.52 ± 0.16		
	23.66									0.53 ± 0.16
	24.48				1.24 ± 0.19				1.06 ± 0.18	
	27.20			1.39 ± 0.21						
	35.36			1.27 ± 0.20					1.00 ± 0.18	
	46.24								0.83 ± 0.17	

‡Nonuniform spatial coverage occurs because of different distance intervals adopted to obtain good average brightness values (given different signal to noise ratios) and because of signal drop-out associated with constraints imposed on positioning the slit profile on the CCD detector during interleaved eclipse and emission measurements.

*Calibration uncertain

TABLE IV
East–West D_2 Brightness Profiles for Sodium Cloud Image Data

UT Date	UT Time	Image ID Number	Io Geocentric Phase Angle (deg)	Io System III Longitude (deg)	East-West Distance from Io for Specified D_2 Brightness Level (satellite radii)							
Image Data Set Reference: Murcray (1978)					0.5 kR		1.0 kR		1.5 kR		2.0 kR	
					Forward	Trailing	Forward	Trailing	Forward	Trailing	Forward	Trailing
1976 Nov. 16	0806	ES 328B	256	262	--	--	51	29	46	24	28	14
1977 Jan 27	0024	ES 369A	86	193	60	38	50	22	44	19	32	16
	0217	ES 370D	102	245	>83	30	56	25	46	21	24	19
Image Data Set Reference: Goldberg(1988†)					0.2 kR		0.5 kR		1.0 kR		2.0 kR	
					Forward	Trailing	Forward	Trailing	Forward	Trailing	Forward	Trailing
1981 May 5	0819	SIP 418/31-33	102	300	78	69	63	40-66	45	37	24	21
May 12	0848	SIP 420/30-32	91	302	66	86	41	37	35	29	20	21
May 13	0346	SIP 421/21-23	253	108	74-103	73	70	41	41	27	29	20
	0555	SIP 421/32-33	271	168	124	65	112	44	51	30	26	19
June 6	0436	SIP 424/10-12	103	300	81	75	68	71	36	26	20	23
Image Data Set Reference: Morgan (1984†)					0.3 kR		0.6 kR		0.9 kR		1.8 kR	
					Forward	Trailing	Forward	Trailing	Forward	Trailing	Forward	Trailing
1983 June 13	0714	i 8492	274	230	--	39	58	26	37	19	20	--
	0722	i 8494	275	233	--	35	52	22	40	20	20	--
	0729	i 8496	276	237	>93	36	52	22	37	17	22	--
	0827	i 8501	284	264	>93	39	61	25	42	19	23	--
	0949	i 8509	296	301	>93	47	63	26	44	17	24	--
	1010	i 8511	299	311	>93	41	63	23	44	16	19	--

†Image observational data obtained by private communication.

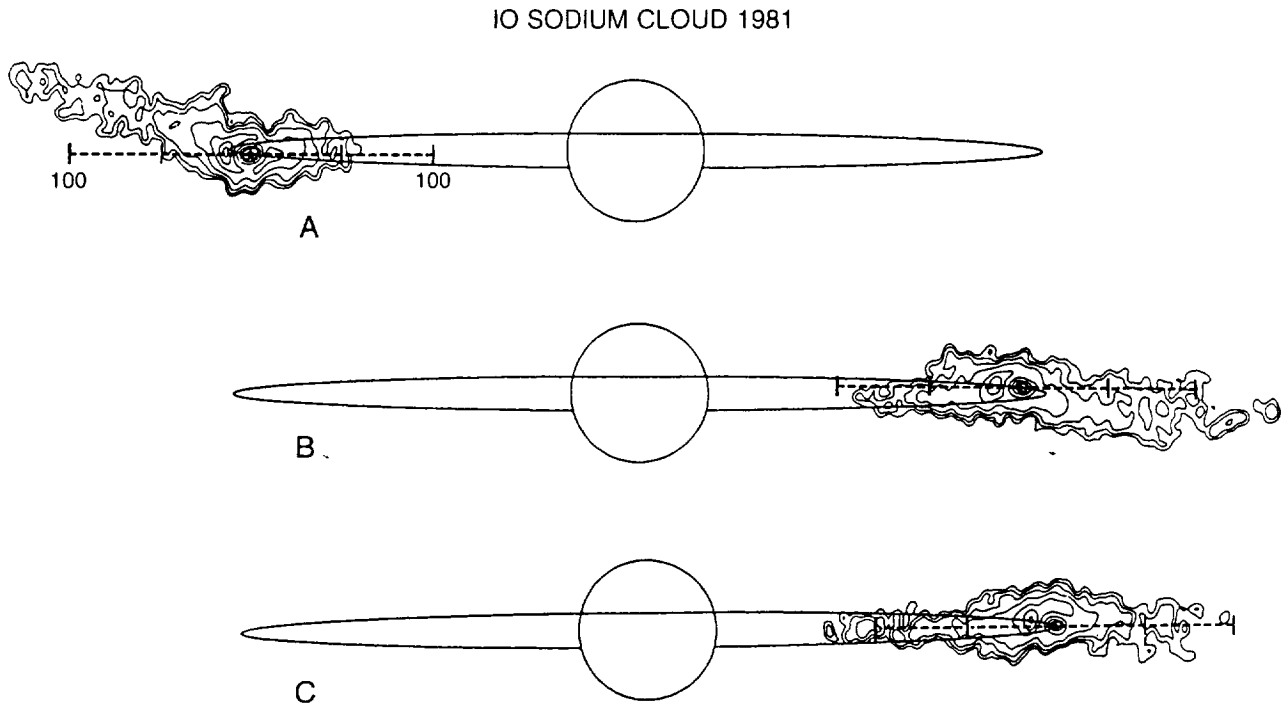

FIG. 1. Io sodium cloud images. Three calibrated D_2 emission images of the Io sodium cloud from the JPL Table Mountain Data Set are shown to proper scale with Jupiter and Io's orbit as viewed from earth in 1981 (Smyth and Goldberg 1993). The Io System III longitude and corresponding orientation of the trailing directional feature in image A are 247° and north, in image B are 104° and south, and in image C are 178° and only very slightly north. An east–west spatial scale of ±100 satellite radii about Io is shown for reference, with tick marks also located at ±50 satellite radii. Contour levels for the D_2 brightness, from outside to inside, are 0.2, 0.5, 1, 2, 4, 6, 8, and 10 kR. An occulting mask of $\sim 10\ R_{Io}$ in radius is centered on Io so that brightness values within this distance are not accurate.

satellite. The forward cloud changes in length, brightness, and east–west orientation relative to the satellite's location as Io moves about Jupiter (i.e., as a function of the Io geocentric phase angle). This change in orientation is well documented (Murcray 1978; Murcray and Goody 1978; Goldberg *et al.* 1984) and is due primarily to the projection upon the two-dimensional sky plane of a three-dimensional cloud (Smyth and McElroy 1978), slightly altered from mirror symmetry by solar radiation pressure (Smyth 1979, 1983), which passes through an east symmetric turning point between about 65° and 85° to 90° and a west symmetric turning point at about 235° (Goldberg *et al.* 1984). A detailed examination of the emission data of Schneider *et al.* (1991), summarized in the last seven columns of Table II, shows that the forward and trailing profiles for the emission data are quite consistent with this known behavior of the Io sodium cloud images. In the trailing cloud, the time-dependent change in the north–south inclination of the fainter directional feature (see Fig. 1) has been shown to be correlated with the System III longitude of Io (Pilcher *et al.* 1984; Goldberg *et al.* 1984) with the directional feature changing from a south to north inclination (a first null point) at an Io System III longitude near 165° and changing from a north to south inclination (a second null point) for a rather poorly defined Io System III longitude somewhere between about 320° and 25°. When the directional feature is near the null location, as illustrated in Fig. 1, an increase in both the spatial extension and brightening of the trailing cloud along the east–west oriented (dashed) line is readily apparent. In addition, since the trailing cloud is associated with a high-speed Io sodium source (~15–20 km sec^{-1}), an increase in the Doppler width of the spectral line in the trailing cloud brightness along an east–west slit is also expected near the null location and is indeed observed in the emission data of Schneider *et al.* (1991), as indicated in Table II.

Information for the sodium D_2 brightness profiles in both the forward and trailing clouds is presented in Fig. 2. The forward and trailing cloud orientation depicted in Fig. 2 is chosen for Io near eastern elongation in order to facilitate the comparison with the 1985 emission data profiles, mostly acquired for Io east of Jupiter. The five emission profiles of Schneider *et al.* (1991) for Io east of Jupiter are shown by different symbol together with their power-law fits ($I_{D_2}(r \geq 4) = Ar^{-\beta}$) given in Table II. For the Io sodium cloud images, the extracted east–west D_2 brightness profiles in Table IV for the forward and trailing clouds are shown by shaded areas, which represent appro-

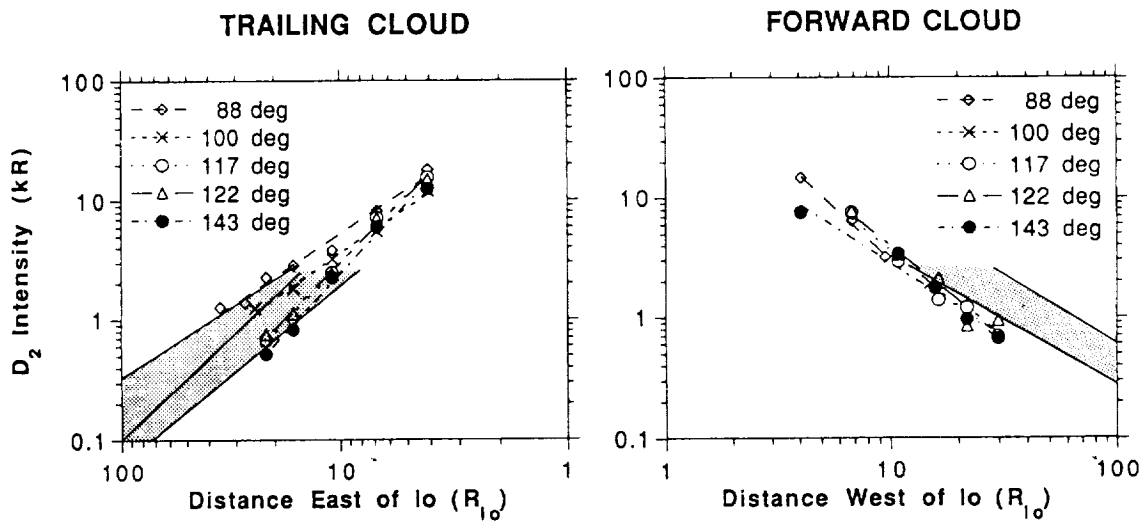

FIG. 2. East and west brightness profiles for selected 1985 emission data and image cloud data. The spatial profiles both east and west of Io for the sodium D_2 emission brightness in units of kilorayleighs are shown as a function of the distance along the observing slit from the center of Io. Five emission observations identified by their satellite geocentric phase angles are shown by the different symbols. These five profiles occur when Io is east of Jupiter and past the satellite phase angle where the forward cloud has its symmetric turning point so that the trailing cloud profiles are all to the east (left) of Io and the forward cloud profiles are all to the west (right) of Io. A power law fit to each profile is also shown. At larger distances from Io, an envelope for the east-west D_2 emission profile acquired from sodium image data is shown by the shaded area. For the trailing profile, the shaded area is divided into two parts: the lower area corresponding to sodium cloud data when the directional feature is oriented either north or south and the upper area corresponding to the directional feature oriented along the east-west direction (i.e., the null condition).

priate bounds for the brightness profiles when Io is somewhat near the elongation points of its orbit. For the trailing cloud, two different shaded areas are shown in Fig. 2 for the two different basic orientations of the directional feature: (1) lower area, when the directional feature is inclined either north or south, and (2) upper area, when the directional feature is at or near the null locations. As expected, the shaded area for the directional feature near the null locations is both brighter and less steep than the shaded area for the directional feature with either a significant north inclination or a significant south inclination. At larger distances from Io (>30 R_{Io}), however, note that both shaded areas for the trailing sodium cloud are dimmer and more closely confined to Io than the shaded area for the forward cloud. In the forward cloud, all the emission brightness profiles are fairly tightly confined and have a slightly steeper slope than the shaded area due to increasing Io geometric plase angle. In the trailing cloud, the brightest and least steep of these profiles is for the emission 4 (Io phase angle 87.7°) acquired for the directional feature at the null condition, while the next brightest profile is for the emission 5 (Io phase angle 100.6°), acquired ~1.5 hr later.

4. ANALYSIS OF THE OBSERVATIONS

Modeling analysis of the one-dimensional sodium distribution described in the previous section will now be undertaken. Collectively, the eclipse measurements for the corona near Io, the emission measurements that extend into the near sodium cloud, and the sodium cloud image derived profiles that reach to distances of $\pm 100\ R_{Io}$, provide a set of spatially overlapping observations that will be used to study and constrain the initial velocity dispersion of the sodium source atoms at the exobase. In the modeling analysis, one-dimensional profiles are calculated using the numerical sodium cloud model of Smyth and Combi (1988a,b), where the electron impact ionization sink for sodium is determined for a 7° tilted corotating plasma torus with an offset-dipole planetary magnetic field in the presence of a nominal (i.e., ~2.8 mV m^{-1} in Io's frame) east–west electric field. A System III longitudinal asymmetry, although present in the torus ion emission, is not included but deferred to a later time when the electron dependence is available.

To investigate the nature of the initial velocity dispersion of the sodium source, two different source flux speed distributions discussed earlier by Smyth and Combi (1988b; see their Appendix D) are considered: (1) a Maxwell–Boltzmann flux distribution and (2) a modified-sputtering flux distribution. The Maxwell–Boltzmann flux distribution $\phi(v; T)$ is based on the Maxwell–Boltzmann velocity distribution and is defined as

$$\phi(v; T) = \phi_0 \left(\frac{R_S}{R_E}\right)^2 \frac{2}{v_\Gamma} \left(\frac{v}{v_T}\right)^3 e^{-(v/v_T)^2} \qquad (1)$$

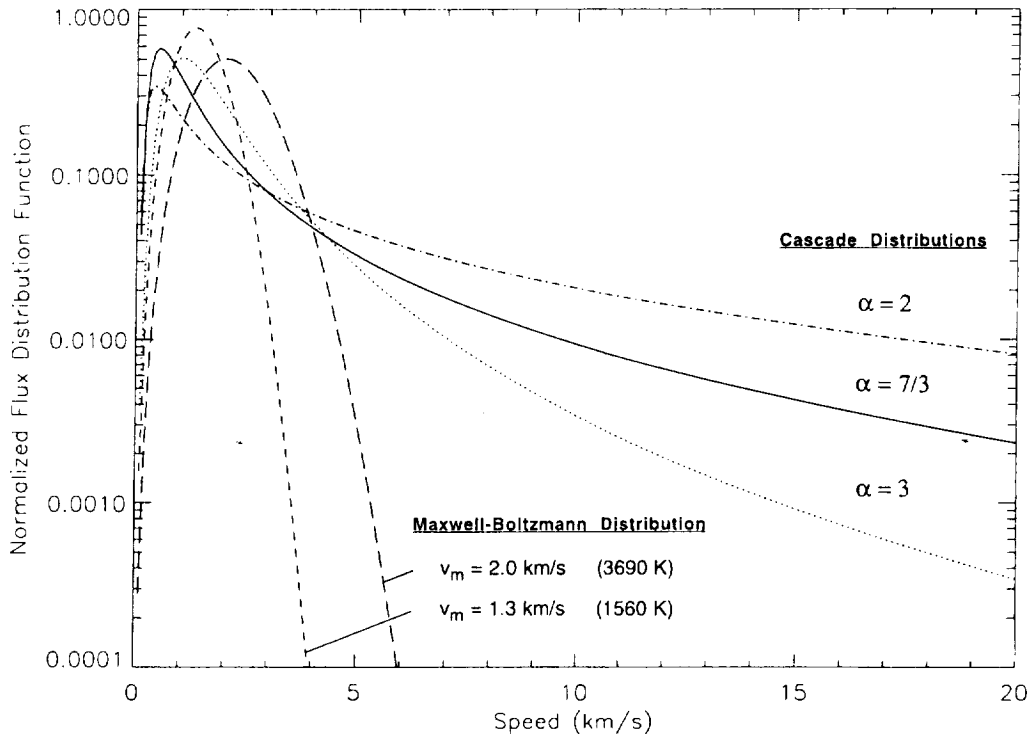

FIG. 3. Flux speed distribution functions for sodium at Io's exobase. Maxwell–Boltzmann flux speed distributions for sodium are shown for most probable speeds, v_m, of 1.3 km sec^{-1} and 2.0 km sec^{-1}. Modified sputtering flux speed distributions are also shown for $\alpha = 3$ and a most probable speed of 1.0 km sec^{-1}, for $\alpha = 7/3$ and a most probable speed of 0.5 km sec^{-1}, and for $\alpha = 2$ and a most probable speed of 0.4 km sec^{-1}. All of the flux speed distributions are normalized to unit area under the curve.

where $v_T = \sqrt{2kT/m}$ is the most probable speed of the velocity distribution for an atom of mass m. The Maxwell–Boltzmann flux distribution is proportional to the local velocity integrated flux ϕ_0 referenced here to the satellite radius R_S not the exobase radius R_E and depends upon one parameter, the exobase temperature T (or alternatively v_T), which determines both the most probable speed $v_m = \sqrt{3kT/m}$ and the speed dispersion of the flux distribution. The modified-sputtering flux distribution $\phi(v; \alpha, v_b, v_M)$ is proportional to the local velocity integrated flux ϕ_0 and depends upon three parameters, an exponent α and two velocity parameters v_b and v_M,

$$\phi(v;\alpha,v_b,v_M) = \phi_0 \left(\frac{R_S}{R_E}\right)^2 \frac{1}{v_b D(\alpha, v_M/v_b)} \left(\frac{v}{v_b}\right)^3 \left(\frac{v_b^2}{v^2+v_b^2}\right)^{\alpha} \left[1 - \left(\frac{v^2+v_b^2}{v_M^2}\right)^{1/2}\right], \quad (2)$$

where $D(\alpha, v_M/v_b)$ is a normalization constant (see Smyth and Combi 1988b). The exponent α primarily determines the dispersion of the distribution, which has a greater high-speed population as α decreases. The exponent α has a value of 3 for a classical sputtering distribution (i.e., a complete collisional cascade process) and a value of 7/3 for a Thomas–Fermi modified-sputtering flux distribution (i.e., the limit of a single elastic collisional ejection process), where the latter distribution is based upon a Thomas–Fermi differential scattering cross section. The velocity parameter v_b is related nonlinearly to the most probable speed v_m of the flux speed distribution and primarily determines v_m (see Smyth and Combi, 1988b, Appendix D). The velocity parameter v_M primarily determines the maximum speed for the flux distribution and depends upon the maximum relative speed (and masses) of the plasma torus ion and sodium atom. For different values of their parameters, two Maxwell–Boltzmann flux distributions and three modified-sputtering flux distributions are shown in Fig. 3 and will be utilized in the subsequent modeling analysis.

In calculating the column density and the D_2 emission brightness in the numerical sodium cloud model, a smaller two-dimensional sky-plane grid centered on Io ($\pm 15\ R_{Io}$) is used to cover a spatial scale near the satellite more appropriate to the eclipse data while a much larger two-dimensional sky-plane grid centered on Io is used to cover a larger spatial scale more appropriate for the emission data and the sodium cloud image data. A one-dimensional profile for the eclipse data is obtained from the smaller

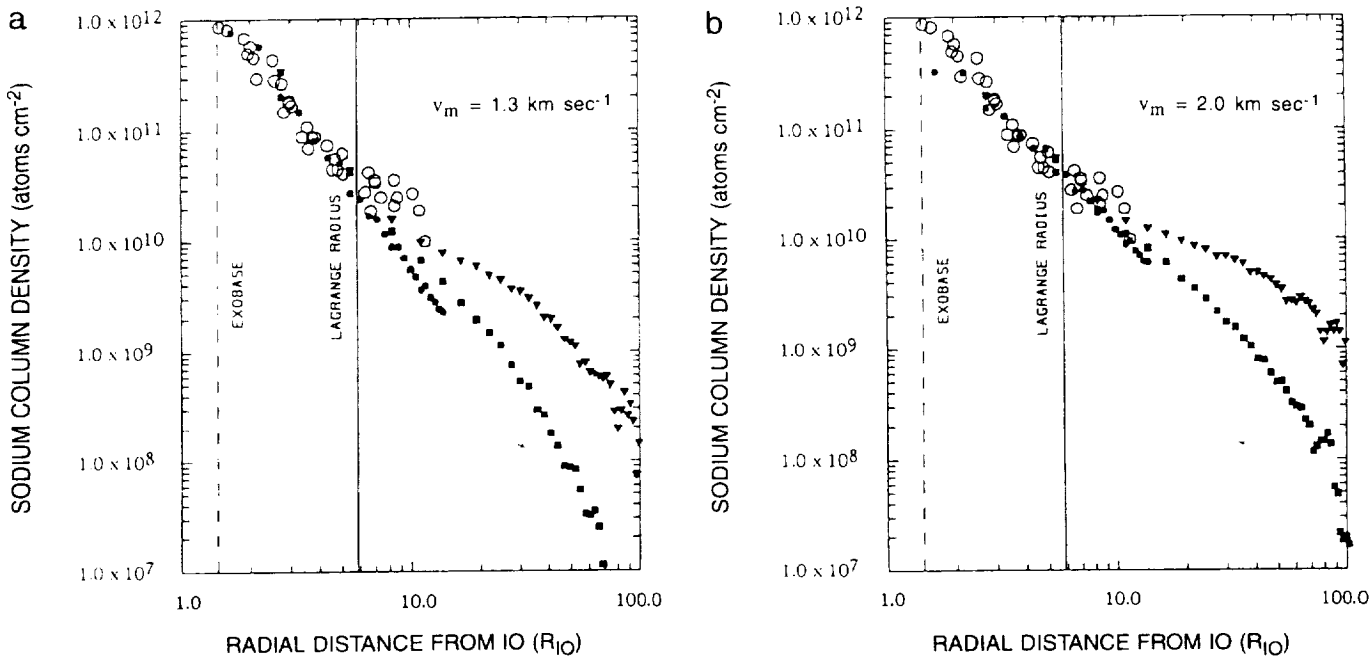

FIG. 4. Model calculations for the Io eclipse data using a Maxwell–Boltzmann flux speed distribution. The atomic sodium column density profile near Io determined from the 1985 eclipse data by Schneider *et al.* (1991) is shown by the open circles. The model calculated column density profiles are shown by solid dots for the (cylindrically averaged) corona, by solid triangles for the forward cloud along the east–west slit direction, and by solid squares for the trailing cloud along the east–west slit direction. These column density profiles were calculated using the Io sodium cloud model of Smyth and Combi (1988b) for their case C description of the plasma torus and for an Io geocentric phase angle of 92.9° and an Io System III longitude angle of 48.6°, which are similar to the emission 4 observation conditions in Table II. Sodium was ejected uniformly from an assumed exobase of 2600 km radius with a velocity dispersion for a Maxwell–Boltzmann flux distribution, where in (a) v_m = 1.3 km sec^{-1} and ϕ_0 = 3.0 × 10^8 atom cm^{-2} sec^{-1}, and in (b) v_m = 2.0 km sec^{-1} and ϕ_0 = 1.8 × 10^8 atom cm^{-2} sec^{-1} (see text).

two-dimensional sky-plane grid by extracting an average radial profile. This average radial profile (called the calculated eclipse profile) will be denoted by the filled circles in Figs. 4–7. A one-dimensional east–west D_2 brightness profile (and also a corresponding column density profile) for the emission data and the sodium cloud image data is obtained from the larger two-dimensional sky-plane grid by selecting only the east–west grid elements that occur in the grid row containing Io. In Figs. 4–7, the calculated east–west brightness and column density profiles are denoted by filled triangles for the forward cloud profile and by filled squares for the trailing cloud profile. To construct an eclipse or east–west profile, monoenergetic model calculations are performed for 18 different nonuniformly spaced speeds ranging from 0.4 to 10 km sec^{-1}. Profiles for speeds beyond 10 km sec^{-1} are determined by an inverse speed extrapolation of the model results. The individual profiles for the different speeds are appropriately weighted for a given source flux speed distribution and then added to obtain the final profile. Model calculations are performed for an Io geocentric phase angle of 92.9° and an Io System III longitude angle of 48.6°. These satellite conditions are similar to those for the emission 4 and eclipse 2 observations of Table II, which are the observations closest to the eastern elongation point. This choice is also appropriate for all the eclipse data, which has no discernible dependence on these two Io related angles, and for the Io sodium cloud image data which have east–west profile areas in Fig. 2 that are representative of the satellite near its orbital elongation points. Modeling analysis results are summarized in Table V and discussed below.

For the first Maxwell–Boltzmann flux distribution in Fig. 3 with a most probable speed of v_m = 1.3 km sec^{-1} (i.e., an exobase temperature of ~1560 K) and with a flux ϕ_0 of 3.0 × 10^8 atoms cm^{-2} sec^{-1} (i.e., a total source of ~1.2 × 10^{26} atoms sec^{-1}), the model calculated eclipse profile (filled circles) in Fig. 4a provides an excellent fit within the Lagrange sphere to the eclipse observations (open circles) and also compares very favorably with the east–west column density profiles calculated for the forward (filled triangle) and trailing cloud (filled squares). This fit verifies and is similar to the earlier 1500 K Maxwell–Boltzmann flux distribution fit of Schneider *et al.* (1991) noted in Section 2. Beyond the Lagrange sphere in Fig. 4a, however, all three of these calculated profiles fall below the eclipse observations, which is considered less accurate

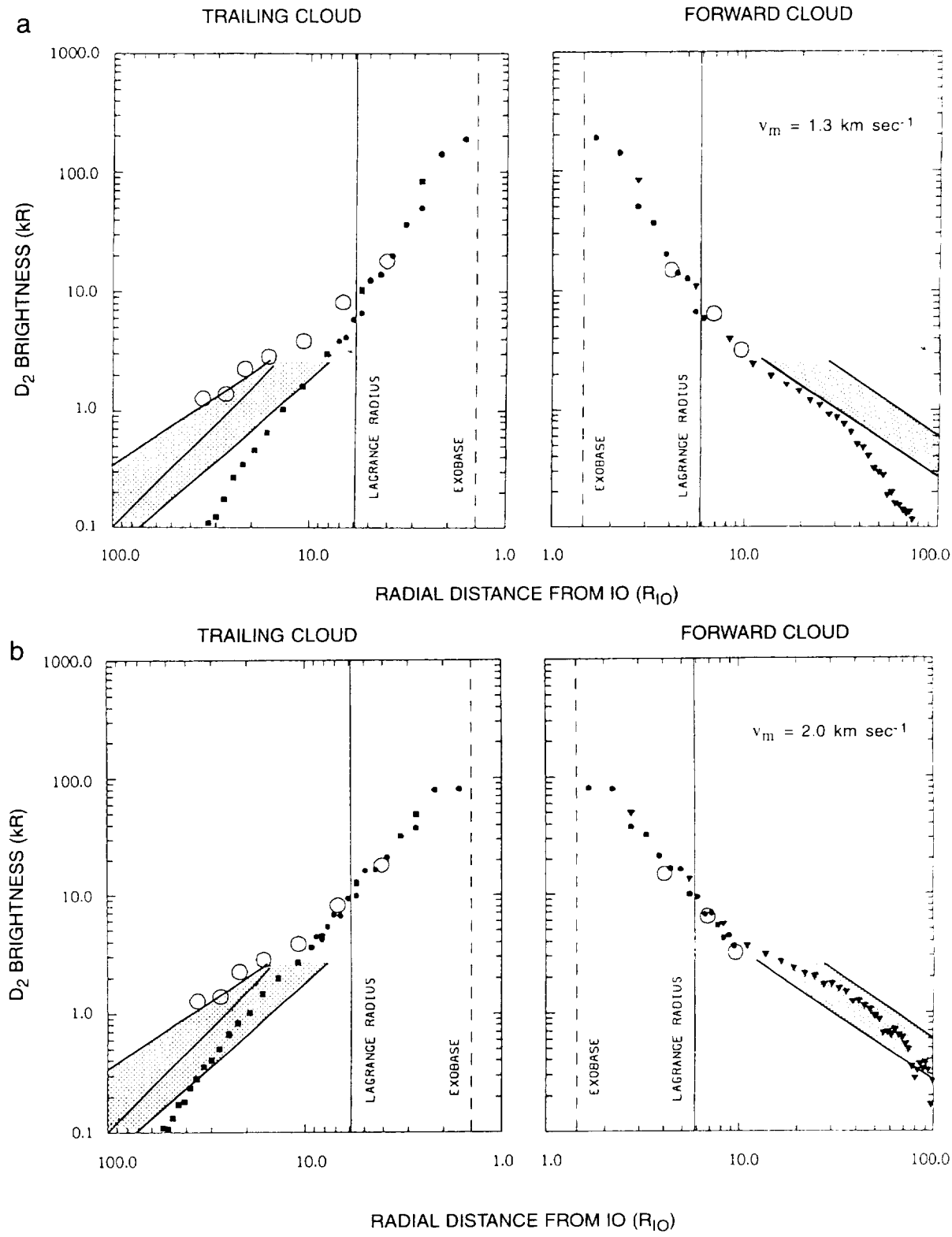

FIG. 5. Model calculations for the east–west D_2 brightness profiles using a Maxwell–Boltzmann flux speed distribution. The east–west D_2 brightness profiles near Io in both the trailing and forward cloud directions as determined by the emission 4 data of Schneider *et al.* (1991) are shown by the open circles. The east–west profile envelopes in both the trailing and forward cloud directions as determined from the sodium cloud image data are shown by the shaded areas (see Fig. 2 caption). The descriptions for the calculated profile symbols, the sodium cloud model and plasma torus, and the Maxwell–Boltzmann flux distribution in (a) and (b) are the same as in the caption of Fig. 4.

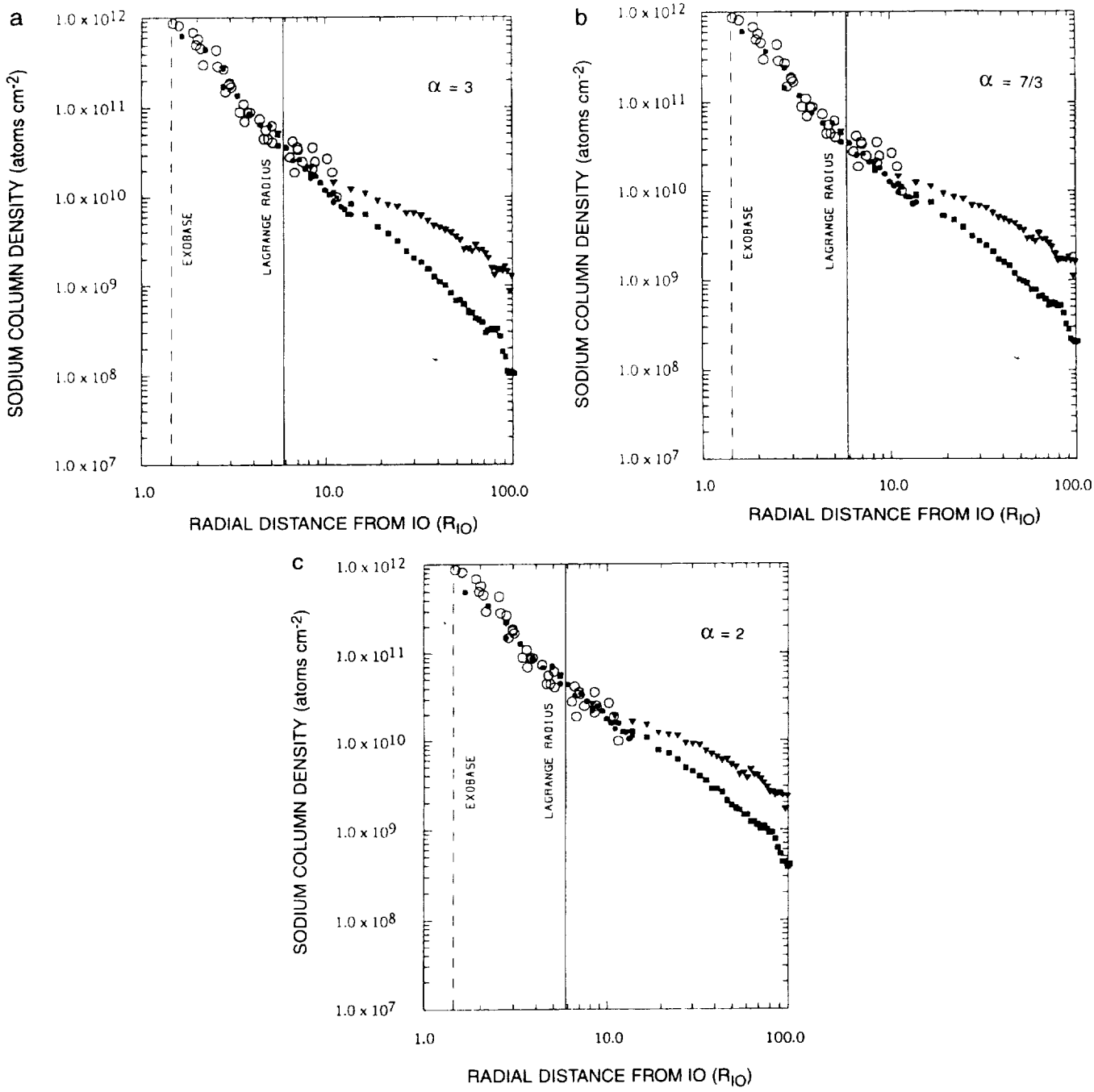

FIG. 6. Model calculations for the eclipse data using a modified sputtering flux speed distribution. The atomic sodium column density profile near Io determined from the 1985 eclipse data by Schneider *et al.* (1991) is shown by the open circles. The model calculated column density profiles are shown by solid dots for the (cylindrically averaged) corona, by solid triangles for the forward cloud along the east–west direction, and by solid squares for the trailing cloud along the east–west direction. These column density profiles were calculated using the Io sodium cloud model of Smyth and Combi (1988b) for their case C description of the plasma torus and for an Io geocentric phase angle of 92.9° and an Io System III longitude angle of 48.6°, which are similar to the emission 4 observation conditions in Table II. Sodium was ejected uniformly from an assumed exobase of 2600 km radius with a velocity dispersion for a modified sputtering flux distribution, where in (a) $\alpha = 3$, $v_m = 1.0$ km sec^{-1}, and $\phi_0 = 3.2 \times 10^8$ atom cm^{-2} sec^{-1}, in (b) $\alpha = 7/3$, $v_m = 0.5$ km sec^{-1}, and $\phi_0 = 4.2 \times 10^8$ atom cm^{-2} sec^{-1}, and in (c) $\alpha = 2$, $v_m = 0.4$ km sec^{-1}, and $\phi_0 = 4.7 \times 10^8$ atom cm^{-2} sec^{-1}.

at these distances. At and beyond about 8 R_{Io}, the calculated east–west forward (filled triangle) and trailing (filled squares) profiles rise above the calculated eclipse profile (filled circles) because the column density is no longer spherically symmetric about Io, with the forward cloud profile having the largest column density and showing a distinct change in its slope compared to the trailing cloud profile. The corresponding model profiles for the D_2 emission brightness are given in Fig. 5a. For both the forward and trailing profiles, the calculated eclipse and calculated east–west profiles are in good agreement with each other inside the Lagrange radius, with a maximum brightness of about 200 kR near the exobase. The calculated east–west profile threads the three emission 4 data points for the forward cloud, but falls well below the emission 4 data points in the trailing cloud. For both the forward and trailing clouds at larger radial distances, the calculated east–west profiles fall well below the areas for both the forward and trailing cloud images. This behavior indicates that there is a large deficiency in the high-speed population for this source flux speed distribution.

Model calculations were therefore performed for the second Maxwell–Boltzmann flux distribution in Fig. 3 with a higher most probable speed of v_m = 2.0 km sec^{-1} (i.e., an exobase temperature of ~3690 K) and with a flux ϕ_0 of 1.8 × 10^8 atoms cm^{-2} sec^{-1} (i.e., a total source of ~0.75 × 10^{26} atoms sec^{-1}) and are shown in Figure 4b and Figure 5b. For the D_2 emission brightness profiles in Figure 5b, the calculated east–west profile now threads the center of the forward cloud image area for a radial distance up to about 70 R_{Io} and the lower trailing cloud image area for a radial distance of about 25 R_{Io} before it falls off too steeply. This improved fit at larger radial distances, however, reduces the D_2 emission brightness at the exobase to about 80 kR in Figure 5b and causes the calculated eclipse profile in Figure 4b to fall below the measured eclipse profile for radial distances inside about 3 R_{Io}. The Maxwell–Boltzmann flux distribution therefore cannot fit both the corona profile near Io and the sodium cloud east–west profiles at large distances from the satellite. A flux distribution that has a broader dispersion with enhanced populations for both the low-speed and high-speed atoms is required. The three modified-sputtering flux distributions in Fig. 3, which have a broader dispersion, are thus

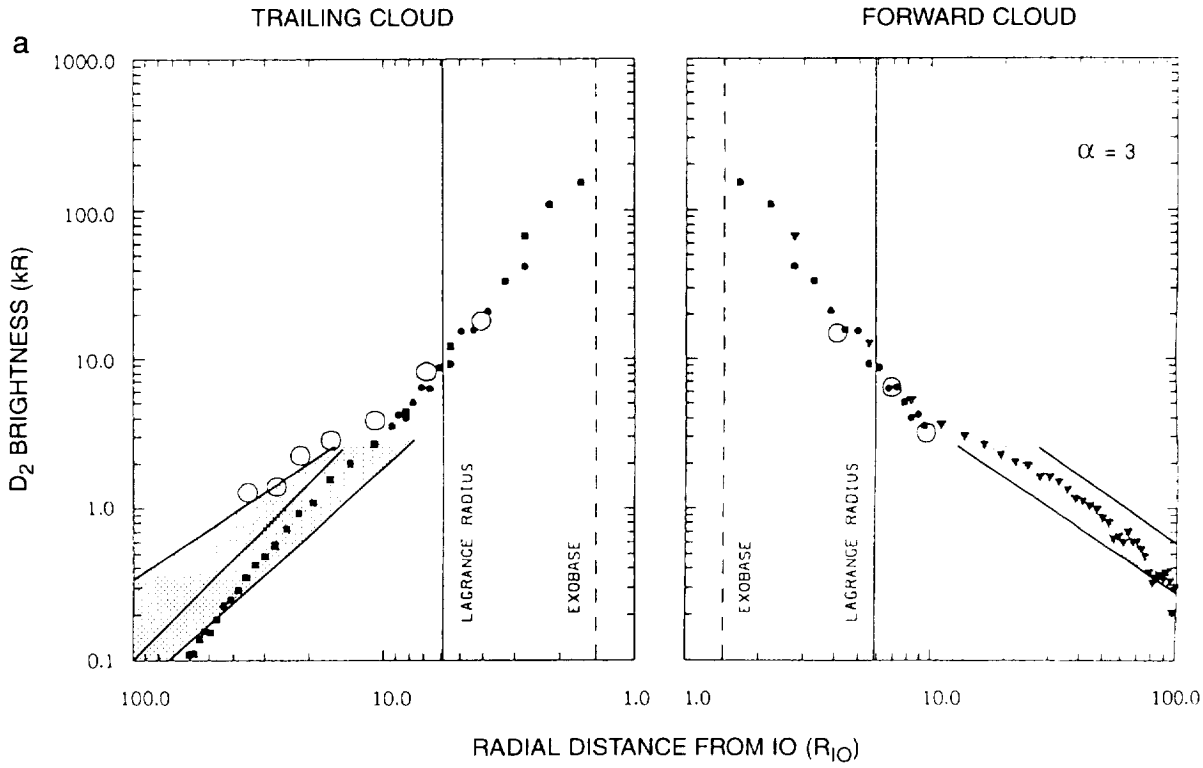

FIG. 7. Model calculations for the east–west D_2 brightness profiles using a modified sputtering flux speed distribution. The east–west D_2 brightness profiles near Io in both the trailing and forward cloud directions determined from the emission 4 data of Schneider *et al.* (1991) are shown by the open circles. The east–west profile envelopes determined from the sodium cloud image data are shown by the shaded areas (see caption of Fig. 2). The descriptions for the calculated profile symbols, the sodium cloud model and plasma torus, and the modified sputtering flux distribution in (a), (b), and (c) are the same as in the caption of Fig. 6.

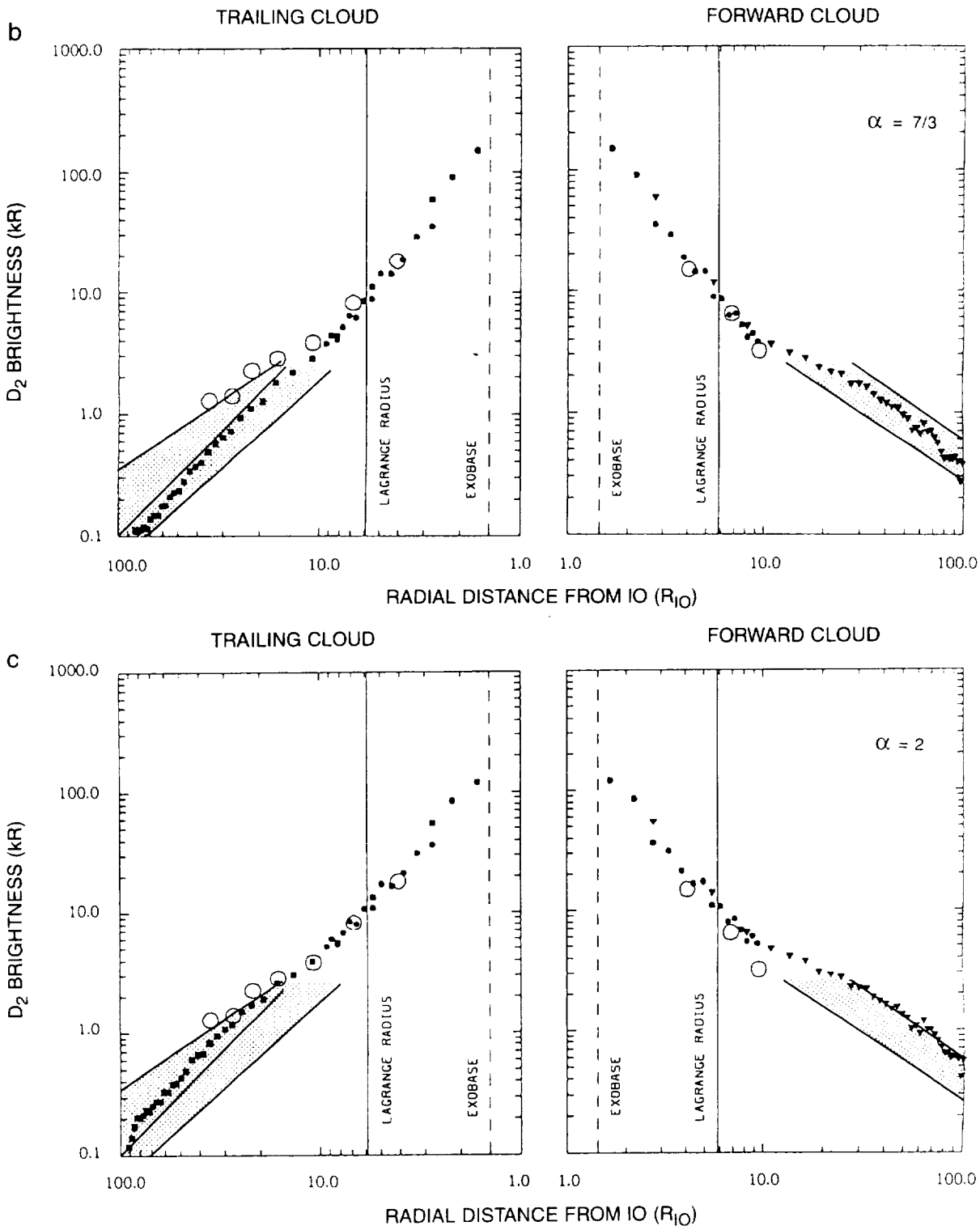

FIGURE 7—*Continued*

TABLE V
Summary Comparison of Modeled and Observed East–West Sodium Profiles for Different Flux Speed Distributions at Io's Exobase

			Corona	Forward Cloud		Trailing Cloud (not null)		Trailing Cloud (null)	
Observations: E/W Radial Interval (R_{Io}):			1.4-6	6-10	10-100	6-10	10-100	6-10	10-100
Distribution Speed Peak (km/s)		Exobase Source Rate (10^{26} atoms/s)	Fits Eclipse Column Profile	Fits Near Io Emission Profile	Fits Far Cloud E/W Profile	Fits Near Io Emission Profile	Fits Far Cloud E/W Profile	Fits Near Io Emission Profile	Fits Far Cloud E/W Profile
1. Maxwell Boltzmann Flux Distribution									
1.3		1.24	YES	YES	too low	little low	too low	too low	too low
2.0		0.75	too low	YES	slightly low	YES	little low	little low	too low
2. Collisional Cascade Flux Distribution									
(classical sputtering)									
$\alpha = 3$	1.0	1.32	YES	YES	tiny low	YES	tiny low	little low	too low
(incomplete cascade: higher velocity tail)									
$\alpha = 7/3$	0.5	1.74	YES	YES	YES	YES	YES	little low	too low
$\alpha = 2$	0.4	1.90	tiny low	too high	too high	too high	too high	YES	YES

considered in the remainder of the paper with model calculations presented in Figs. 6 and 7.

Model calculations for a classical sputtering flux distribution ($\alpha = 3$) and a modified-sputtering flux distribution ($\alpha = 7/3$) are presented in Figs. 6a and 6b for the eclipse observations and in Figs. 7a and 7b for the east–west D_2 emission brightness profiles. For these two flux distributions, the most probable speeds are, respectively, 1.0 km sec^{-1} and 0.5 km sec^{-1}, and the sodium fluxes ϕ_0 are, respectively, 3.2×10^8 atoms cm^{-2} sec^{-1} (i.e., a total source of $\sim 1.3 \times 10^{26}$ atoms sec^{-1}) and 4.2×10^8 atoms cm^{-2} sec^{-1} (i.e., a total source of $\sim 1.7 \times 10^{26}$ atoms sec^{-1}). From the exobase to radial distances of ~ 8 R_{Io}, just beyond the Lagrange radius, both sputtering flux distributions provide a very good fit in Figs. 6a and 6b to the observed eclipse column density profile (open circles) and correspond to an exobase D_2 emission brightness of about 150 kR in Figs. 7a and 7b. For the classical sputtering flux distribution in Fig. 7a, the calculated D_2 emission brightness profile for the forward profile is slightly above the measured data point (open circles) inside the Lagrange radius, matches the two measured data points beyond the Lagrange radius, and then threads the forward cloud image area nicely between about 20 R_{Io} and 80 R_{Io} before it falls too rapidly and drops below this area. An excellent fit for the forward profile is, however, provided by the modified sputtering distribution ($\alpha = 7/3$) in Fig. 7b where the calculated D_2 emission brightness profile matches the measured data points (open circles) both inside and beyond the Lagrange radius as well as nicely threading the forward cloud image area all the way to 100 R_{Io}. For the trailing cloud, the calculated D_2 emission brightness profile for the classical sputtering flux distribution in Fig. 7a matches the measured data point inside the Lagrange radius, is slightly below the two measured data points outside the Lagrange radius, and then threads the lower of the two trailing cloud image areas nicely between about 15 R_{Io} and 35 R_{Io} before it falls too rapidly and drops below this area. An excellent fit for the trailing profile is, however, provided by the modified sputtering distribution ($\alpha = 7/3$) in Fig. 7b where the calculated D_2 emission brightness matches the measured data point inside the Lagrange radius, is slightly below the two measured data points outside the Lagrange radius, and then threads the lower (non-null) trailing cloud image area nicely all the way to 100 R_{Io}. It is particularly noteworthy that the isotropic ejection of sodium from the exobase with a modified sputtering flux distribution with $\alpha = 7/3$ provides a complete fit to the combined eclipse, emission, and forward/trailing sodium cloud image profile data for this non-null condition from 1.4 to 100 R_{Io}.

In order to fit the trailing cloud (upper area) profile for the directional feature at the null condition, it is then clear that a flux distribution is required with an even more enhanced higher-speed population (~ 20 km sec^{-1}) than the modified sputtering flux distribution with $\alpha = 7/3$. Since the modified sputtering flux distribution for $\alpha = 7/3$ corre-

sponds to the limit of a single collision cascade process described by a Thomas–Fermi cross section (see Smyth and Combi 1988b), reducing the value of α to a smaller value becomes somewhat physically questionable but will be used here for the purposes of simply illustrating the impact of a more enhanced higher-speed sodium population in the model calculation. As discussed earlier, this higher-speed sodium is thought to be nonisotropically ejected from Io's exobase and attributed to some combination of direct collisional and lower-velocity charge exchange ejection. Choosing the modified sputtering flux distribution with $\alpha = 2$ in Fig. 3 which has a most probable speed of 0.4 km sec^{-1} and selecting an isotropic exobase source rate of 1.9×10^{26} atoms sec^{-1} (i.e., a flux ϕ_0 of 4.7×10^8 atoms cm^{-2} sec^{-1}), the model-data comparison is shown in Fig. 6c for the eclipse column density and in Fig. 7c for the east–west D_2 emission brightness. The sputtering flux distribution provides a reasonably good fit to the observed column density data points in Fig. 6c with only a small departure very near the exobase and produces a column density profile beyond 10 R_{Io} that is significantly enhanced compared to the $\alpha = 7/3$ case in Fig. 6b. In Fig. 7c, this enhancement in the forward cloud is obvious, where the calculated D_2 emission brightness profile is significantly above the measured data points both inside and outside the Lagrange radius and is above or in the very top of the forward cloud image area all the way to 100 R_{Io}. The additional enhanced high-speed population of the $\alpha = 2$ modified sputtering flux distribution is too large and therefore not consistent with the observed forward profile. In contrast for the trailing cloud in Fig. 7c, the calculated D_2 emission brightness profile matches the measured data points inside and outside of the Lagrange radius very well and then threads the upper of the two trailing cloud image areas nicely all the way to ~90 R_{Io}. This demonstrates that the trailing cloud can be fitted with an enhanced higher-speed population of sodium atoms in the flux distribution. It also immediately demonstrates that the flux distribution at the exobase must be nonisotropic with the enhanced high-speed population weighted toward vector directions that will preferentially populate the trailing cloud. As discussed in Section 2, this nonisotropic requirement for a flux distribution for speeds of ~20 km sec^{-1} is similar to the conclusions reached by earlier modeling analyses (Pilcher *et al.* 1984; Smyth and Combi 1991; Wilson and Schneider 1995).

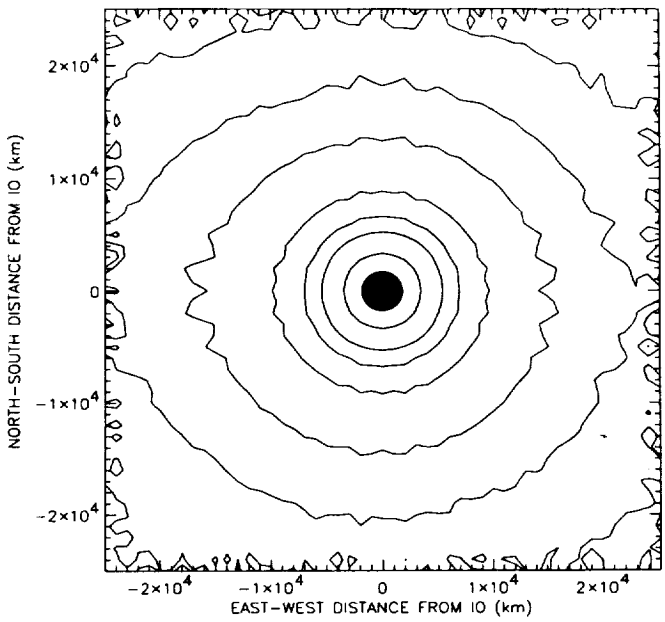

FIG. 8. Two-dimensional nature of the sodium column density near Io. Contours for the two-dimensional column density near Io are shown in the sky-plane of the earth as determined from the sodium cloud model calculation for the modified sputtering flux speed distribution described in Fig. 6(b) for $\alpha = 7/3$. The vertical and horizontal directions are the projected directions that are, respectively, perpendicular and parallel to the semimajor axis of the Io's orbital ellipse on the sky plane. Io's location and size are shown to scale by the black circle. The sodium column density contours in units of 10^{11} atoms cm^{-2} are, from inside to outside, 5, 2, 1, 0.5, 0.2, 0.1, and 0.05.

5. DISCUSSION AND CONCLUSIONS

The composite spatial information for sodium obtained by combining the eclipse observations (radial distances from Io of 1.4 to ~10 R_{Io}), the emission observations (east–west distances of ±4 to ±30–40 R_{Io}), and the sodium cloud observations (east–west distances of ±10 to ±100 R_{Io}) has been analyzed to extract a basic description for the flux speed distribution at the satellite's exobase. An isotropic modified-sputtering flux speed distribution in Fig. 3 with $\alpha = 7/3$, a most probable speed of 0.5 km sec^{-1}, and a source strength of 1.7×10^{26} atoms sec^{-1} provides a very good fit to these composite observations when the directional feature is either north or south and hence not contributing to the east–west profile of the trailing cloud. It is remarkable that these observations, acquired by a number of ground-based programs over very different spatial scales and at different times during the 1976–1985 decade, are so self-consistent. Near Io, the two-dimensional sodium column density produced by this modified sputtering distribution as calculated by the sodium cloud model in the profile analysis above is shown in Fig. 8 and can be seen at larger distances from Io to become nonspherical and more confined near the satellite plane. This flattening near the satellite plane is the merging of the near Io corona into the sodium cloud and is caused naturally by orbital dynamics beyond the satellite Lagrange sphere where the gravity of Jupiter is dominant. The forward cloud portion of the east–west emission data profiles has a rather tightly confined slope that, in the absence of the trailing cloud

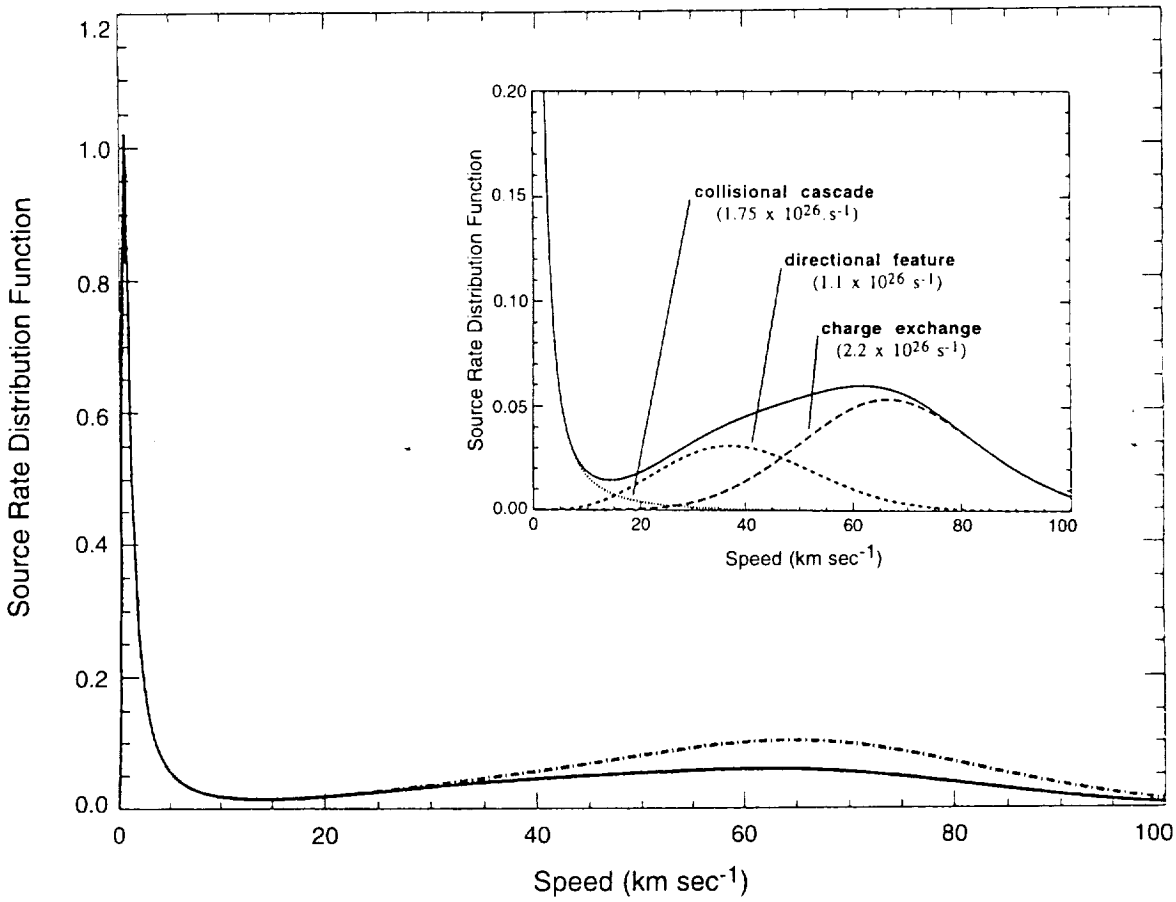

FIG. 9. Total source rate speed distribution function for sodium at Io's exobase. The total source rate speed distribution function at Io's exobase, in units of 10^{26} atoms sec^{-1} (km/sec)$^{-1}$, is composed of three separate source rate speed distributions as discussed in the text and is shown for two different source strengths for the higher-speed zenocorona source centered about 57 km sec^{-1}. The lower (solid line) and upper (dashed-dot line) curves correspond, respectively, to the sodium zenocorona higher-speed source rates of 2.2×10^{26} atoms sec^{-1} (Smyth and Combi 1991) and 4×10^{26} atoms sec^{-1}. The two source rates for the higher-speed zenocorona source are shown to exhibit its typical time-variable source strength range of $\sim 2\text{–}4 \times 10^{26}$ atoms sec^{-1} as reported by Flynn *et al.* (1994). The decomposition of the solid curve into its three separate source rate speed distributions is shown in the cutout and is determined by combining (1) the isotropic modified sputtering source rate distribution (dotted line in the cutout) for $\alpha = 7/3$, $v_m = 0.5$ km sec^{-1} and a source strength of 1.7×10^{26} atom sec^{-1}, (2) the nonisotropic lower-speed source rate distribution (short dashed line in the cutout) for the sodium zenocorona and directional feature centered about 20 km sec^{-1}, with a source strength of 1.1×10^{26} atoms sec^{-1} as determined by Smyth and Combi (1991), and (3) the nonisotropic higher-speed source rate distribution (longer dashed line in the cutout) for the sodium zenocorona centered about 57 km sec^{-1}, with a charge exchange source strength of 2.2×10^{26} atoms sec^{-1} as determined by Smyth and Combi (1991).

enhancement at the null condition, is less steep and is brighter than the trailing cloud profiles. In order, however, to reproduce the extended east–west profile in the trailing sodium cloud when the directional feature is in the satellite plane (i.e., the null location), additional nonisotropic high-speed sodium is required.

The sodium atoms ejected from Io's exobase as described above by the modified sputtering flux distribution have speeds primarily in the range from 0 to a few tens of km sec^{-1}. This neutral flux distribution represents the spatially integrated effect of the incomplete collisional cascade process that occurs from the collisional interactions of heavy ions in the corotating plasma torus with neutrals in Io's atmosphere. This flux speed distribution can be alternatively described as a source rate speed distribution by multiplying it by the satellite surface area. In addition to these ion-neutral elastic collisional encounters, resonance charge exchange between plasma torus sodium ions and neutral sodium in Io's atmosphere is also responsible for producing a sodium source with higher speeds relative to Io. These speeds are centered about the corotational ion speed ($\sim$57 km sec^{-1}) relative to Io's motion and have a dispersion reaching from several tens of km sec^{-1} to $\sim$100 km sec^{-1}. Such high speed sodium ($\leq$80 km sec^{-1}) has

recently been observed near Io by Cremonese *et al.* (1992). As discussed in Section 2, this higher-speed nonisotropic source of sodium together with the lower speed (~15–20 km sec^{-1}) nonisotropic source for the directional feature form the source for the sodium zenocorona or magnetonebula. Earlier modeling studies (Smyth and Combi 1991; Flynn *et al.* 1992) indicated that the higher-speed source was $\sim 2 \times 10^{26}$ atoms sec^{-1} while the lower speed source was $\sim 1 \times 10^{26}$ atoms sec^{-1}. More recent observations and analysis (Flynn *et al.* 1994) have shown that the higher-speed sodium source is time variable and in the range ~ 2–4×10^{26} atoms sec^{-1}. A total source rate speed distribution for sodium at Io's exobase has hence been constructed by combining the modified sputtering source rate distribution determined in this paper with the two source rate distribution for the zenocorona as given by Smyth and Combi (1991) and is shown in Fig. 9. The lower (solid line) and upper (dashed-dot line) curves correspond, respectively, to the sodium zenocorona higher-speed source rates of 2.2×10^{26} and 4×10^{26} atoms sec^{-1}. Total source rate speed distribution functions at Io's exobase expected for other atomic species, such as K, O, and S, can be constructed in a similar fashion by adopting the estimated source rates given by Smyth and Combi (1991).

Future studies for the sodium flux speed distribution at Io's exobase are anticipated using much larger data sets now available for east–west and north–south sodium emission observations. It will then be possible to analyze the combined spatial and spectral information and refine the nonisotropic nature of the flux distribution and also to search for other possible east–west and System III related variations. Once this information is determined for sodium, the implications for the more abundant species in Io's atmosphere will be particularly important in other related studies for the many-faceted and complex phenomena in the Io–Jupiter system.

ACKNOWLEDGMENTS

We are grateful to N. M. Schneider for helpful discussions and for providing the numerical data for the 1985 emission observations. We also thank the two referees for their helpful comments. This research was supported by the Planetary Atmospheres Program of the National Aeronautical and Space Administration under Grant NAGW-3585 to the University of Michigan and under Contracts NASW-4416, NASW-4471, and NASW-4804 to Atmospheric and Environmental Research, Inc.

REFERENCES

Bergstralh, J. T., D. L. Matson, and T. V. Johnson 1975. Sodium D-line emission from Io: Synoptic observations from Table Mountain Observatory. *Astrophys. J. Lett.* **195,** L131–L135.

Bergstralh, J. T., J. W. Young, D. L. Matson, and T. V. Johnson 1977. Sodium D-line emission from Io: A second year of synoptic observation from Table Mountain Observatory. *Astrophys. J. Lett.* **211,** L51–L55.

Brown, R. A. 1974. Optical line emission from Io. In *Exploration of the Planetary System* (A. Woszczyk and C. Iwaniszewska, Eds.), Proceedings IAU Symposium No. 65, Torun, Poland, Sepetember 5–8, 1973, pp. 527–531. Reidel, Dordrecht.

Brown, R. A., and Y. L. Yung 1976. Io, its atmosphere and optical emissions. In *Jupiter: Studies of the Interior, Atmosphere, Magnetosphere, and Satellites* (T. Gehrels, Ed.), pp. 1102–1145. Univ. of Arizona Press, Tucson.

Carlson, R. W., D. L. Matson, and T. V. Johnson 1975. Electron impact ionization of Io's sodium emission cloud. *Geophys. Res. Lett.* **2,** 469–472.

Cremonese, G., N. Thomas, C. Barbieri, and C. Pernechele 1992. High resolution spectra of Io's neutral sodium cloud. *Astron. Astrophys.* **256,** 286–298.

Fang, T.-M., W. H. Smyth, and M. B. McElroy 1976. The distribution of long-lived gas clouds emitted by satellites in the outer Solar System, *Planet. Space Sci.* **25,** 577–588.

Flynn, B. 1993. Oscillating ion streamline model of Jupiter's neutral sodium nebula. *Adv. Space Science* **13,** 325–330.

Flynn, B., M. Mendillo, and J. Baumgardner 1992. Observations and modeling of the jovian remote sodium emission. *Icarus* **99,** 115–130.

Flynn, B., M. Mendillo, and J. Baumgardner 1994. The jovian sodium nebula: Two years of ground-based observations. *J. Geophys. Res.* **99,** 8403–8409.

Goldberg, B. A., R. W. Carlson, D. L. Matson, and T. V. Johnson 1978. A new asymmetry in Io's sodium cloud, *Bull Am. Astron. Soc.* **10,** 579.

Goldberg, B. A., Yu. Mekler, R. W. Carlson, T. V. Johnson, and D. L. Matson 1980. Io's sodium emission cloud and the Voyager 1 encounter. *Icarus* **44,** 305–317.

Goldberg, B. A., G. W. Garneau, and S. K. LaVoie 1984. Io's sodium cloud. *Science* **226,** 512–516.

Ip, W.-H. 1990. Neutral gas–plasma interaction: The case of the plasma torus, *Adv. Space Res.* **10,** 15–23.

Macy, W. W., Jr., and L. M. Trafton 1980. The distribution of sodium in Io's cloud: Implications. *Icarus* **41,** 131–141.

Matson, D. L., B. A. Goldberg, T. V. Johnson, and R. W. Carlson 1978. Images of Io's sodium cloud. *Science* **199,** 531–533.

Mendillo, M., J. Baumgardner, B. Flynn, and W. J. Hughes 1990. The extended sodium nebula of Jupiter. *Nature* **348,** 312–314.

McGrath, M. A. 1988. *Ion Bombardment of Io and Mercury.* Ph.D. Thesis, Dept. of Astronomy, University of Virginia.

Murcray, F. J. 1978. *Observations of Io's Sodium Cloud.* Ph. D. Thesis, Dept. of Physics, Harvard University.

Murcray, F. J., and R. M. Goody 1978. Pictures of the Io sodium cloud. *Astrophys. J.* **226,** 327–335.

Pilcher, C. B., W. H. Smyth, M. R. Combi, and J. H. Fertel 1984. Io's sodium directional features: Evidence for a magnetospheric-wind-driven gas escape mechanism. *Astrophys. J.* **287,** 427–444.

Schneider, N. M. 1988. *Sodium in Io's Extended Atmosphere.* Ph.D. Thesis, Department of Planetary Sciences, Univ. of Arizona.

Schneider, N. M., D. M. Hunten, W. K. Wells, and L. M. Trafton 1987. Eclipse measurements of Io's sodium atmosphere. *Science,* **238,** 55–58.

Schneider, N. M., D. M. Hunten, W. K. Wells, A. B. Schultz, and U. Fink 1991. The structure of Io's corona. *Astrophys. J.* **368,** 298–315.

Sieveka, E. M., and R. E. Johnson 1984. Ejection of atoms and molecules from Io by plasma-ion impact. *Astrophys. J.* **287,** 418–426.

Smyth, W. H. 1979. Io's sodium cloud: Explanation of the east–west asymmetries. *Astrophys. J.* **234,** 1148–1153.

SMYTH, W. H. 1983. Io's sodium cloud: Explanation of the east-west asymmetries. II. *Astrophys. J.* **264,** 708–725.

SMYTH, W. H., AND M. R. COMBI 1987a. Correlating east-west asymmetries in the jovian magnetosphere and the Io sodium cloud, *Geophys. Res. Lett.* **14,** 973–976.

SMYTH, W. H., AND M. R. COMBI 1987b. Time variability of the sodium cloud, poster paper at the international conference "Time-Variable Phenomena in the Jovian System," Flagstaff, Arizona, August 25–27.

SMYTH, W. H., AND M. R. COMBI 1987c. Nature of Io's atmosphere and its interaction with the planetary magnetosphere. *Bull. Am. Astron. Soc.* **19,** 855.

SMYTH, W. H., AND M. R. COMBI 1988a. A general model for Io's neutral gas cloud. I. Mathematical description. *Astrophys. J. Supp.* **66,** 397–411.

SMYTH, W. H., AND M. R. COMBI 1988b. A general model for Io's neutral gas clouds. II. Application to the sodium cloud. *Astrophys. J.* **328,** 888–918.

SMYTH, W. H., AND M. R. COMBI 1991. The sodium zenocorona. *J. Geophys. Res.* **96,** 22711–22727.

SMYTH, W. H., AND B. A. GOLDBERG 1993. The Io sodium cloud: Space-time signatures of east-west and system III longitudinal asymmetries in the jovian magnetosphere. Paper presented at Io: An international conference, San Juan Capistrano, California, June 22–25.

SMYTH, W. H., AND M. B. MCELROY 1977. The sodium and hydrogen gas clouds of Io, *Planet. Space Sci.* **25,** 415–431.

SMYTH, W. H., AND M. B. MCELROY 1978. Io's sodium cloud: Comparison of models and two-dimensional images. *Astrophys. J.* **226,** 336–346.

SUMMERS, M. E., D. F. STROBEL, Y. L. YUNG, J. T. TRAUGER, AND F. MILLS 1989. The structure of Io's thermal corona and implications for atmospheric escape. *Astrophys. J.* **343,** 468–480.

TRAFTON, L., AND W. MACY, JR. 1978. On the distribution of sodium in the vicinity of Io, *Icarus* **33,** 322–335.

WILSON, J. K., AND N. M. SCHNEIDER 1994. Io's fast sodium: Implications for molecular and atomic atmospheric escape, *Icarus* **111,** 31–44.

WILSON, J. K., AND N. M. SCHNEIDER 1995. Io's sodium directional feature: Evidence for ionospheric rip-off, *Bull. Am. Astron. Soc.* **27,** 1154.

JOURNAL OF GEOPHYSICAL RESEARCH, VOL. 103, NO. A5, PAGES 9071-9081, MAY 1, 1998

Io's plasma environment during the Galileo flyby: Global three-dimensional MHD modeling with adaptive mesh refinement

M. R. Combi, K. Kabin, T. I. Gombosi, and D. L. DeZeeuw
Space Physics Research Laboratory, University of Michigan, Ann Arbor

K. G. Powell
Department of Aerospace Engineering, University of Michigan, Ann Arbor

Abstract. The first results for applying a three-dimensional multiscale ideal MHD model for the mass-loaded flow of Jupiter's corotating magnetospheric plasma past Io are presented. The model is able to consider simultaneously physically realistic conditions for ion mass loading, ion-neutral drag, and intrinsic magnetic field in a full global calculation without imposing artificial dissipation. Io is modeled with an extended neutral atmosphere which loads the corotating plasma torus flow with mass, momentum, and energy. The governing equations are solved using adaptive mesh refinement on an unstructured Cartesian grid using an upwind scheme for MHD. For the work described in this paper we explored a range of models without an intrinsic magnetic field for Io. We compare our results with particle and field measurements made during the December 7, 1995, flyby of Io, as published by the Galileo Orbiter experiment teams. For two extreme cases of lower boundary conditions at Io, our model can quantitatively explain the variation of density along the spacecraft trajectory and can reproduce the general appearance of the variations of magnetic field and ion pressure and temperature. The net fresh ion mass-loading rates are in the range of ~300-650 kg s^{-1}, and equivalent charge exchange mass-loading rates are in the range ~540-1150 kg s^{-1} in the vicinity of Io.

1. Introduction

Io's interaction with Jupiter's corotating inner magnetosphere has been studied for over 25 years. Io has a neutral atmosphere which is probably locally thick but rather uneven across its surface [*Lellouch et al.*, 1992; *Ballester et al.*, 1994]. The ultimate source for atmospheric gases appears to be the numerous active volcanoes on the surface. It is the energetic particle environment near Io which is responsible for the balance of the plasma heating, Joule heating, ionization, and surface and atmospheric sputtering, and which in some form drives the escape of the neutral atmosphere [*Schneider et al.*, 1989]. A realistic model for the flow of magnetospheric plasma, interacting with Io's neutral atmosphere is necessary for a complete understanding of the global picture.

The results of the measurements by the particle and field instruments on the Galileo Orbiter during the December 1995 flyby of Io provide new and important information with which a realistic MHD simulation for the plasma interaction can be tested. *Kivelson et al.* [1996a,b] have recently suggested that an intrinsic magnetic field for Io with a strength and direction which would nearly cancel the local Jovian field near the surface of Io, can explain many aspects of the Galileo magnetometer measurements taken during the December 1995 flyby of Io. However, the large plasma densities and low temperatures measured at the same time by the Galileo plasma science package [*Frank et al.*, 1996] and the plasma wave instrument [*Gurnett et al.*, 1996], indicate that ion mass loading is significant and may provide an explanation for the magnetic field measurements without requiring an intrinsic field.

Our understanding of the interaction of Io with Jupiter's magnetosphere goes back to the discovery of Io-related decametric radio emission discovered by *Bigg* [1964] and the unipole inductor model which explains it [*Goldreich and Lynden-Bell* 1969]. There have been a number of theoretical studies of this interaction during the immediate post-Voyager era [e.g., *Southwood et al.*, 1980; *Neubauer*, 1980] (see also *Hill et al.* [1983] for an excellent post-Voyager review). *Neubauer* [1980] presented an analytical model of Alfvén standing wave current system which connects current through the ionosphere of Io. *Southwood et al.* [1980] examined data from several Voyager instruments and examined the possible role of an intrinsic magnetic field for Io as a way to retain a robust enough ionosphere to provide enough conductivity for completing the Io-Jupiter current circuit. Early theoretical work was often done either in the context of a "thin" atmosphere [e.g., see *Cloutier et al.*, 1978] indicative of the surface temperature (~130 K), or "thick" extended neutral atmosphere [e.g., see *Goertz*, 1980] more indicative of volcanic

Paper number 98JA00073.
0148-0227/98/98JA-00073$09.00

temperatures (~1000 K). Subsequent evidence [*Sieveka and Johnson*, 1985; *Schneider et al.*, 1991; *Lellouch et al.*, 1992; *Ballester et al.*, 1994; *Belton et al.*, 1996] seems to indicate a mixed picture of the global atmosphere, which has a large extended corona like a thick atmosphere, but appears to be dominated by local major injection of hot (high speed) gas/dust plumes to high altitudes but only near active volcanic vents. Therefore, although the atmosphere is probably only locally thick, it still has a large extended neutral corona which might provide a sufficient source of impact ionization and photoionization.

There have been a number of three-dimensional (3-D) numerical studies of the plasma flow past Io [*Linker et al.*, 1988, 1989, 1991; *Wolf-Gladrow et al.*, 1987]. Because of the complexities in the problem and numerical difficulties, studies have been limited to restricted portions of the problem, have introduced fixes such as artificial viscosity, or have been run using less than fully physically realistic conditions. *Linker et al.* [1991] have performed the best example to date of 3-D MHD modeling of Io. In this model they used the two-step Lax-Wendroff method. These calculations were performed on a nonuniform but fixed structured grid, and artificial dissipative terms (artificial viscosity) had to be introduced to the basic MHD equations in order to make them computational stable.

A new numerical method has been developed at the University of Michigan for solving the full 3-D MHD equations which resolves a number of difficulties that have plagued past attempts. The 3-D version of this new method, called multiscale adaptive upwind scheme for MHD (MAUS-MHD), has already been applied to the full comet-solar wind interaction problem and has been discussed in detail by *Gombosi et al.* [1996]. This interaction is quite similar to that expected for the Io-Jupiter-magnetosphere interaction in the absence of an intrinsic magnetic field for Io. A full Earth magnetosphere version of the same calculation has also recently been developed [*De Zeeuw et al.*, 1996], so the method is also able to treat intrinsic magnetic fields as well, if necessary. We can and have run test cases with an intrinsic field for Io, but in this paper, concentrate on trying to explain the existing data with nonintrinsic field models.

2. Model Description

In the 3-D MAUS-MHD model the calculation is done on an unstructured Cartesian grid using octree adaptive mesh refinement (AMR). This makes optimal use of computer resources allowing problems with disparate scales and unusual and varying geometries to be modeled globally, while still retaining sufficient resolution locally to capture shocks and other important features resulting from naturally occurring sharp gradients in the flow. The octree structure is a hierarchical cell structure, based on multiple generations of cubic parent cells which can be split into eight daughter cells. The adaptive data structure has been explained by *DeZeeuw and Powell* [1992]. The approximate eight-wave Riemann solver for ideal MHD is combined with a second-order MUSCL-type scheme [*van Leer*, 1979]. It uses a novel approach to handle the "div **B** problem" derived and discussed at length by *Powell* [1994] and *Powell et al.* [1995, also Multiscale adaptive upwind scheme for magneto-hydrodynamics; MAUS-MHD, manuscript in preparation, 1998]. In this scheme div **B**/r is treated as a passive scalar so that any numerically generated nonzero contributions are convected away. Once div **B** = 0 is imposed as an initial condition to the problem it is satisfied to within truncation error.

Our model of Io's interaction with Jupiter's magnetosphere is essentially similar to the comet problem of *Gombosi et al.* [1996]. The dimensionless conservative form of the ideal MHD equations can be written as

$$\frac{\partial \tilde{\mathbf{W}}}{\partial \tilde{t}} + \left(\nabla \cdot \tilde{\mathbf{F}}\right) = \tilde{\mathbf{S}} \tag{1}$$

where W and S are eight-dimensional state and source vectors, while F is an 8 x 3 dimensional flux diad. All quantities denoted by a tilde are normalized by physical quantities in the undisturbed upstream region

$$\tilde{t} = a_\infty t / R_{Io} \tag{2a}$$

$$\tilde{\mathbf{r}} = \mathbf{r} / R_{Io} \tag{2b}$$

$$\tilde{\rho} = \rho / \rho_\infty \tag{2c}$$

$$\tilde{\mathbf{u}} = \mathbf{u} / a_\infty \tag{2d}$$

$$\tilde{p} = p / \rho_\infty a_\infty^2 \tag{2e}$$

$$\tilde{\mathbf{B}} = \mathbf{B} / \sqrt{\mu_0 \rho_\infty a_\infty^2} \tag{2f}$$

where t is time, $\boldsymbol{r}$ is radius vector, ρ is mass density, $\boldsymbol{u}$ is bulk flow velocity, p is pressure, μ_0 is the permeability of free space, and $\boldsymbol{B}$ is magnetic field vector. The subscript ∞ refers to values in the undisturbed upstream flow. Finally, R_{Io} is the radius of Io and a_∞ is the hydrodynamic sound speed in the undisturbed upstream plasma flow.

The normalized state and flux vectors are written as

$$\tilde{\mathbf{W}} = \begin{pmatrix} \tilde{\rho} \\ \tilde{\rho}\tilde{\mathbf{u}} \\ \tilde{\mathbf{B}} \\ \tilde{\varepsilon} \end{pmatrix} \tag{3a}$$

$$\tilde{\mathbf{F}} = \begin{pmatrix} \tilde{\rho}\tilde{\mathbf{u}} \\ \tilde{\rho}\tilde{\mathbf{u}}\tilde{\mathbf{u}} + \left(\tilde{p} + \frac{1}{2}\tilde{B}^2\right)\mathbf{I} - \tilde{\mathbf{B}}\tilde{\mathbf{B}} \\ \tilde{\mathbf{u}}\tilde{\mathbf{B}} - \tilde{\mathbf{B}}\tilde{\mathbf{u}} \\ \tilde{\mathbf{u}}\left(\tilde{\varepsilon} + \tilde{p} + \frac{1}{2}\tilde{B}^2\right) - \left(\tilde{\mathbf{B}} \cdot \tilde{\mathbf{u}}\right)\tilde{\mathbf{B}} \end{pmatrix} \tag{3b}$$

where $\tilde{\varepsilon}$ is the normalized internal energy density

$$\tilde{\varepsilon} = \frac{1}{2}\left[\tilde{\rho}\tilde{\mathbf{u}} \cdot \tilde{\mathbf{u}} + \frac{2\tilde{p}}{\gamma - 1} + \tilde{B}^2\right] \tag{4}$$

The source vector in (1) corresponding to ion mass-loading, $\dot{M}$, is of the same form as used by *Gombosi et al.* [1996], and is given in normalized units as

$$\tilde{S}=\begin{pmatrix} \dot{M} \\ \left(\dot{M}+\eta\tilde{\rho}\right)\tilde{u}_n-\eta\tilde{\rho}\tilde{u} \\ 0 \\ \frac{1}{2}\left(\dot{M}+\eta\tilde{\rho}\right)\tilde{u}_n{}^2-\eta\left(\frac{1}{2}\rho\tilde{u}^2+\frac{1}{\gamma-1}\tilde{p}\right) \end{pmatrix}, \quad (5)$$

where

$$\dot{M}=\frac{m_c}{\rho_\infty}\frac{R_{Io}}{a_\infty}Q_i\left(\frac{R_{Io}}{r}\right)^\alpha,$$

$$\eta=\frac{R_{Io}}{a_\infty}F_{in}\left(\frac{R_{Io}}{r}\right)^\alpha.$$

Q_i is the ionization rate per unit volume evaluated at Io's radius; F_{in} is the ion-neutral collision momentum-energy transfer rate per unit volume, also evaluated at Io's radius. In the simplest interpretation $Q_i(R_{Io}/r)^\alpha$ is given by the neutral density, n_n, divided by τ_i, the ionization timescale for neutrals, and $F_{in}(R_{Io}/r)^\alpha$ is given by $n_n k_{in}$, where k_{in} is the ion-neutral momentum transfer collision rate, and n_n is the neutral density. The choice for the exponent, α, is discussed below. For the Io cases presented here the net neutral flow velocity, u_n, is taken to be zero. This could be generalized in the future to account for a net escaping neutral atmosphere at high altitudes.

For the Io version of the MAUS-MHD model simulations were performed both for a pure conducting sphere with and without ion mass loading and for a sphere with fixed boundary conditions, as discussed in detail below. The simulation volume is 900 x 600 x 600 R_{Io}, and there are 9 levels of refinement and 92,000 cells with sizes ranging from < 0.1 R_{Io} near Io to 50 R_{Io} far upstream and downstream. We have chosen the upstream plasma conditions as follows from our best estimates of the Galileo December 1995 epoch, including the various recently published Galileo measurements (see Table 1). Since the calculation is performed in normalized units, there is some flexibility to rescale the results over a range of realistic conditions, but this cascades to other parameters [see, e.g., *Gombosi et al.*, 1996]. We have investigated numerous versions of cases for a simple conducting sphere, a mass-loading ionosphere, and with an intrinsic magnetic field for Io.

The formulation of mass loading for comets [*Gombosi et al.*, 1996] permits us to incorporate both the effects of mass loading from new ionization (impact and photoionization) as well as momentum and energy loading from charge exchange and nonreactive ion-neutral collisions. In the comet calculation Gombosi et al. used the term "ion-neutral friction" to describe the effect of collisions which cause momentum and energy exchange but which result in no new ions. The dominant source of such an exchange of momentum and energy results from symmetric charge exchange reactions involving the dominant torus ions and atmospheric neutrals (O^+ + O, S^+ + S, and S^{++} + S). *Linker et al.* [1991] appropriately included an ion mass loading rate and a "charge exchange rate" in their MHD models. However, many nonreactive collisions between ions and atmospheric neutrals also can exchange momentum and energy without yielding net new ion mass. These so-called knock-on collisions are important for producing the extended neutral corona of Io [*Sieveka and Johnson*, 1985; *Johnson*, 1990]. Furthermore, it has been shown by *Smyth and Combi* [1997] that the distribution of sodium in the corona [*Schneider et al.*, 1991] as well as the more familiar B-cloud is a natural outcome of the collisional cascade process (incomplete atmospheric sputtering) that is initiated by such collisions. For simplicity in the remainder of this paper this momentum-energy loading term is referred to as the charge exchange rate.

On the basis of Voyager-era conditions, *Smyth* [1992] has estimated a total collision rate of ~2 x 10^{28} s^{-1} between incident plasma torus ions and neutrals in Io's atmosphere with about 1/3 yielding fresh ions deposited into the plasma flow and the rest contributing to momentum/energy exchange alone, i.e., the charge exchange rate. These estimates are based on extrapolations of knowledge gained about the extended sodium atmosphere of Io to the more abundant neutral species S, O, SO, and SO_2. On the basis of their own estimates, *Linker et al.* [1989, 1991] have explored MHD models with a comparable charge-exchange rate but with a fresh ion mass-loading rate nearly an order of magnitude smaller (~10^{27} s^{-1}) than Smyth's. Based on the then non-detection of optical/UV emissions close to Io, *Shemansky* [1980] provided an upper limit to the fresh ion mass-loading rate of ~10^{27} s^{-1}. *Smyth and Shemansky* [1983] later raised this to 4 x 10^{27} s^{-1} after subsequent detections of neutral O and S emissions from ground-based and space-based remote measurements. It is also likely that the torus is more robust in recent years, and that mass, momentum, and energy input rates may all be higher now than 17 years ago. This appears to be borne out by comparisons between Galileo measurements during the December 1995 flyby and Voyager measurements [*Frank et al.*, 1996; *Gurnett et al.*, 1996].

As is evidenced by the range of values which appear in the literature, making an independent estimate for ion mass loading and charge exchange rates is difficult, because they are based on a number of uncertain and indirect measurements and assumptions. With the availability of the Galileo PLS measurements [*Frank et al.*, 1996] of plasma density, temperature, and pressure we have adopted the different approach of using the net ion mass-loading and charge exchange rates as adjustable parameters and constraining the values based on comparison of our model results with the measurements along the spacecraft track.

SO_2 appears to be the major primary constituent in Io's atmosphere [*Ballester et al.*, 1994; *Lellouch et al.*, 1992], but observations still to date only provide hemispherically

Table 1. Upstream Plasma Conditions

Parameter	Value
Upstream plasma density	3500 cm^{-3}
Upstream plasma temperature	92 eV
Upstream mean molecular mass	22 amu
Upstream magnetic field	1800 nT
Corotation flow speed	56.8 km s^{-1}
Alfvénic Mach number	0.4
Mach number	2.2
Ratio of specific heats (γ)	1.667

averaged total column abundances. The sodium eclipse measurements of *Schneider et al.* [1991] are the only unambiguous information we have about the vertical distribution of neutral gas species in the corona of Io from about 1.4 to about 6 R_{Io}. The interpretation of recent Hubble observations of various UV emissions of atomic S and O [*Ballester et al.*, 1996] is complicated by the fact that the spatial distributions of the emissions are determined by a combination of the mass distribution in the atmosphere with excitation by the plasma density and temperature environment. Theoretical and empirical models have explored the structure of the neutral atmosphere and its behavior to various gas sources and energetic heating and ejection processes, such as sublimation, volcanic ejection, surface and atmospheric sputtering, UV, plasma, and Joule heating, and LTE and non-LTE IR radiative cooling [*Sieveka and Johnson*, 1985; *McGrath and Johnson*, 1987; *Moreno et al.*, 1991; *Strobel et al.*, 1994; *Pospiezalska and Johnson*, 1996; *Wong and Johnson*, 1995; *Smyth and Combi*, 1997]. Despite recent advances in observational and theoretical work, still only a rough sketch of the structure of the neutral atmosphere can be made.

For our MHD simulations we have adopted ion mass, momentum, and energy loading source terms in the vicinity of Io as if proportional to the neutral density distribution which is scaled as a power law in distance (r/R_{Io}) with an exponent, α. We do not need to specify the neutral density itself, however, just the ionization mass and momentum/energy exchange rates and their dependence on distance. We have adopted the power law with an exponent of $\alpha \sim -3.5$ as found by *Schneider et al.* [1991] for the trace species, sodium, outside about 1.4 R_{Io}. *Smyth and Combi* [1997] have shown that this vertical distribution of sodium from the *Schneider et al.* [1991] eclipse observations and the more typical emission profiles of more spatially extended sodium can together be explained by a single modified incomplete cascade sputtering distribution, which results naturally from multiple neutral-neutral and ion-neutral collisions between torus ions and atmospheric neutrals. Therefore it is reasonable to expect a similar type distribution for neutral species in general. This power law is contrasted with the less steep inverse square-type power law distribution assumed in past MHD mass-loading calculations [*Linker et al.*, 1988, 1991]. For the mass-loading models presented here, we assume the neutral distribution has this dependence from an inner boundary at 150 km above the surface of Io, out to the Lagrange radius of 6 R_{Io}.

If details about the ion composition and electron temperature in the torus, and the global spatial distribution and composition of the neutral atmosphere were available, it would be possible to make a better estimate of the spatial distribution of the ion mass-loading rate and the charge-exchange rate (the collisional energy-momentum loading rate) needed to specify the source terms in the MHD equations. Typical cross sections [*McGrath and Johnson*, 1989] between oxygen and sulfur ions dominating the torus and O, S, and SO_2 neutrals dominating the atmosphere show that typical symmetric charge exchange reactions have cross sections in the range of 20 to 40 $Å^2$ whereas most impact ionization and elastic collisions [*Johnson*, 1990] have cross sections in the range of 1 to 20 $Å^2$. Electron impact of course only nets ion mass but is highly dependent on the electron temperature.

The power law distribution may not be correct well inside of 1.4 R_{Io} because the range of the observations of *Schneider et al.* [1991] started at this distance. At much lower altitudes the resulting ion mass-loading rate is a trade off between the likely rapid increasing of neutral density (probably more like an exponential scale height distribution), with the decreasing plasma flux (electron and ions) caused by recombination and plasma-neutral collisions themselves. *Flaser et al.* [1997] have shown preliminary results of Galileo radio occultation measurements which indicate electron densities in excess of 50,000 cm^{-3} at the peak of the ionosphere, ~50-80 km above the surface. This is similar to but higher than given by *Kliore et al.* [1974, 1975] from the Pioneer era, and again generally consistent with the more robust torus of the recent times. At this time, a fully coupled MHD-ionosphere calculation would be beset with many assumptions, for example, the neutral atmosphere density profile which is still uncertain to within a factor of a few. In any case the scope of this type of study is currently beyond the state of the art even for the Earth for which there is much more knowledge.

For the models presented in this paper we have adopted two types of lower boundary conditions which represent opposite pictures of the type of conditions present above Io's ionosphere. One is a perfectly conducting impenetrable sphere. In this case both the magnetic field and the plasma flow are reflected from the lower boundary. This represents an extreme case of not allowing either plasma flow or magnetic flux to penetrate the sphere, and we hereafter refer to this as a reflecting boundary condition. The second case corresponds to fixed boundary conditions where the magnetic field and plasma density and velocity are specified in ghost cells just below the boundary. In this case both magnetic flux and plasma flow can pass through the boundary. For the fixed boundary condition model presented here the plasma density is set to a value of 3 times the upstream torus density (or 10,500 cm^{-3}) which is representative of the global spherical average indicated by radio occultation measurements at an altitude of 150 km. The plasma velocity is set to zero, being consistent with strong coupling to the neutral atmosphere. The choice of a value for the fixed magnetic field at the lower boundary requires some discussion. We hereafter refer to this case as fixed boundary conditions.

Linker et al. [1991] presented model results which solved for the full MHD equations (mass, momentum, energy, and B field) outside of Io, and only the magnetic field with a constant conductivity inside the inner boundary, throughout the interior of Io. The internal conductivity was set in such a way to obtain a high enough integrated conductivity (10-150 mhos) necessary for maintaining the Jupiter-Io current system. They point out that it is not really known where the current loops close, i.e., in the ionosphere but outside of Io, or even through the dense lower ionosphere and into a possible conducting interior. Linker et al. found, however, that the same exterior solutions could be obtained whether they performed the computationally intensive calculation of the magnetic field inside Io or whether they simply held the B field at the inner boundary constant at the background level. In fact, their full calculation showed that in any case "the magnetic field changed very little inside the sphere."

The physical interpretation for a constant magnetic field is that if Io does not have an intrinsic B field (i.e., from an internal dynamo), it would be expected that a value similar to the average imposed Jovian external field would be induced over time. We have estimated that the time-averaged value of the field at Io happens to be slightly less (~98%) than the

instantaneous value at Io's position at the point of Galileo's close approach. The same ratio was found either roughly using the variation from the old *Goertz et al.* [1976] magnetic field model or more carefully using the newest model of *Connerney et al.* [New model of Jupiter's magnetic field constrained by the Io flux tube footprint, manuscript in preparation, 1998]. It is noteworthy that those models predict values that are overall too low and too high, respectively, compared with the actual values measured by Galileo [*Kivelson et al.*, 1996b].

As mentioned already for this study we have left the ion mass-loading rate and the charge exchange rate (pure momentum/energy exchange) as adjustable parameters. We then undertook an iterative procedure to vary these quantities and compare our model results with the measured plasma density, pressure, and magnetic field along the Galileo spacecraft trajectory until a reasonable (albeit not perfect) match was obtained. Upstream we assume the aforementioned torus conditions. Downstream and to the sides of the simulation box we assume absorbing boundary conditions, i.e., mass, momentum, and energy, exit, and nothing comes back. Because of the adaptive grid technology we are able to place the upstream, downstream, and lateral boundaries far enough from Io so they do not affect on the solution.

3. Model Results

To serve as a baseline, we show results for a perfectly conducting sphere without mass loading, given realistic upstream plasma torus conditions. We refer to this case as no mass loading and reflective boundary conditions. This is shown mainly for comparison with the similar nonintrinsic field model of *Kivelson et al.* [1996b], and to serve as a point of comparison with the mass-loaded cases. For this case, the only parameters to be set are the upstream Mach number of 2.2 and the upstream Alvénic Mach number of 0.4. In (5) the ion-mass and ion-neutral drag rates Q_i and F_{in} are zero. The results are scaleable to other values of upstream magnetic field and conducting radius given constraints imposed by the Mach number (which does not have a great effect on the overall global structure of the flow) and the Alfvénic Mach number (which is more critical). In any case our estimates of both the upstream Mach number and Alfvénic Mach number are consistent with the measured Galileo flyby conditions and rigid corotation.

We show results for two mass-loading cases where the particular values of the ion mass-loading rate and the charge-exchange rate serve as the adjustable parameters. We have run some models with larger exponents (-4 to -5), however, -3.5 is based on an actual measurements and is quite satisfactory. The goal is to be able to reasonably reproduce the variation of the plasma density, pressure (and temperature), and magnetic field along the spacecraft trajectory according to the results of the Galileo Io flyby results [*Frank et al.*, 1996; *Kivelson et al.*, 1996b; *Gurnett et al.*, 1996]. The sensitive features in the plasma data to be reproduced are (1) the height of the plasma density peak along the center of the wake, (2) the reduction of the magnetic field, (3) total width of the disturbance in all quantities, (4) the reversal and side peaks of the pressure and temperature, and (5) the vector velocity magnitude and direction. *Frank et al.*, [1996] have reported plasma velocities (44 km s^{-1}) that are below corotational speeds (56.8 km s^{-1}) even 4 R_{Io} from the central axis of the wake. However, these have a large enough uncertainty (-5 and +15 km s^{-1}) to be consistent with corotational speed, which seems more reasonable.

Plates 1a-1f show a comparison of slices of the magnetic field and flow streamlines in the planes parallel and perpendicular to the upstream magnetic field for the non-mass-loaded and both mass-loaded cases. In the non-mass-loaded reflective case one can see the strong influence of the Alfvén wings in the parallel plane (1a) [see *Neubauer*, 1980; *Linker et al.*, 1991] as the flow diverts around the conducting sphere and as the disturbance is directed off at the expected angle (tan $\theta = 1/M_A$) where θ is the deflection angle and M_A is the Alfvénic Mach number. In MHD the Alfvén wings are the analog of vortex sheets of regular fluid dynamics [*Kogan*, 1961]. In the parallel plane for the mass-loading case with reflective boundary conditions (1b), the effect of the inner boundary conducting sphere, which dominates the non-mass-loaded case, is weakened but still present. Finally, in the fixed-boundary mass-loading case (1c) the effect of the Alfvén wings has all but disappeared. Plates 1d-1f show the comparable plots in the plane perpendicular to the upstream magnetic field. The December 1995 Galileo flyby trajectory lay very close to this plane. The diverted flow streamlines are not very different between any of the three cases, in fact for the two mass-loaded cases the flow fields in this plane are virtually identical. The small variations in the magnetic field magnitude are apparent. Note that in mass-loading fixed case (Plates 1c and 1f) the diversion of flow is similar in both planes.

Plates 2a, 2b & 2c show the striking differences for the plasma ion density among the various cases. The dark lines show the outlines of the octree cell structure of the adaptively refined mesh. In the non-mass-loading reflective case (2a) the flow diversion around the sphere is evident. The density concentrates somewhat along the Alfvén wings but the wake is essentially evacuated of material. The mass-loaded reflective case (2b) shows a large density pileup in the wake right behind Io and a fair dispersion of material spread in the direction parallel to the upstream magnetic field. This is caused by the strong influence of the reflective boundary conditions. The mass-loaded fixed boundary case (2c) also produces a plasma wake, but it is more concentrated along the central line of the wake, does not have the large extension along the field-parallel direction (as in Plate 2b), and is more extended along the wake.

Direct comparisons of the model with the Galileo flyby data, along the trajectory are given in Figures 1a-1d. Model results are superimposed on the measurements for both mass-loading models with reflective and fixed boundary conditions. The reduction of the magnetic field in the wake along the spacecraft trajectory is shown in Figure 1a. Both of these models provide a similar breath and depth of the magnetic field disturbance as the pure intrinsic dipole model of *Kivelson et al.*, [1996b]; i.e., the measured field disturbance is wider and deeper. The model with reflective boundary conditions yields a somewhat deeper central disturbance than the fixed boundary model, but the overall widths are nearly identical.

Figure 1b shows the plasma density compared with the measurements of *Frank et al.* [1996]. Both the peak of the density at the center of the wake and the width of the disturbance are well reproduced by both mass-loading models. In fact, the height of the plasma density was one key factor in adjusting the mass-loading rate in our process of reproducing the measurements. The plasma pressure from the model is

compared with the Frank et al. data in Figure 1c and the temperature in Figure 1d. The character of the pressure/ temperature disturbance is reasonably well reproduced. There is a rise to either side of a narrow central minimum. The depth and width of the central minima in pressure and temperature, which correspond well with narrow density peak, are well reproduced by both models. However, the measurements show a large increased temperature and pressure in the flanks of the wake, which roughly corresponds to the wider measured magnetic field disturbance, and which is not quantitatively reproduced by either mass-loading model. The models show smaller peaks which are closer to the central line of the wake, and the model with reflecting boundary conditions produces higher side peaks in both temperature and pressure.

The two key attributes on which we focused fitting were the height of the density peak (as mentioned above) and the central depth of the minima in temperature and pressure. Although there is some interplay in adjusting both parameters, the density peak was more sensitive to changes in the mass-loading rate, while the depths of the pressure and temperature minima were more sensitive to the charge exchange rate. For the model results shown in Plates 1 and 2 and Figure 1, the total ion mass-loading rate corresponds to 0.84 x 10^{28} and 1.8 x 10^{28} ions s^{-1} for the fixed and reflective boundary condition models, respectively, where the mean molecular mass is 22 amu and the radial distribution varied as $r^{-3.5}$. The charge exchange rate (due again to momentum/energy loading for which charge exchange is the dominant part) is equivalent to 1.5 x 10^{28} and 3.2 x 10^{28} ions s^{-1}, respectively, for comparison with the charge exchange rates given by *Linker et al.* [1991]. For the best match to the density peak and pressure reversal, the ion-neutral collision frequency was about two times the ionization rate. The 2 to 1 ratio in relative rates are in rough agreement with recent estimates by *Smyth* [1992].

This net ion mass loading corresponds to a fresh ion mass-loading rate of 300-650 kg s^{-1}. From the momentum/energy exchange rate we can generate an equivalent total apparent mass-loading rate which has contributions from both the true ionization rate as well as the momentum and energy loading from the combination of (mostly) symmetric charge exchange and non-reactive ion-neutral collisions of about 840-1800 kg s^{-1}. This total loading rate is a factor of 2-4 larger than Smyth's

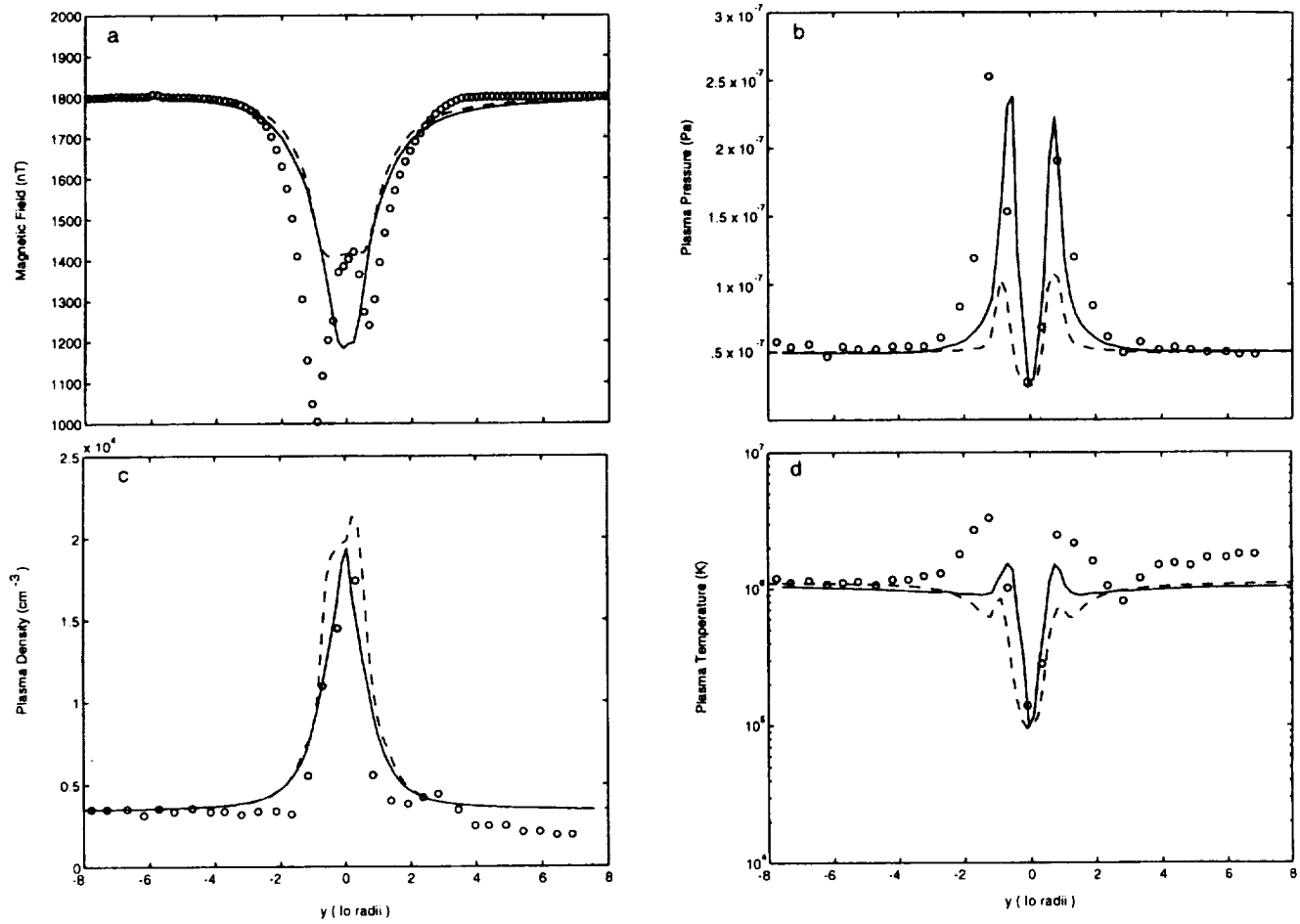

Figure 1. Comparison of the mass-loading models with Galileo particle and field measurements. The magnetic field measurements in (a) from *Kivelson et al.* [1996] are shown with the model values. The (b) plasma density, (c) pressure, and (d) temperature from the model are shown with those from *Frank et al.* [1996] obtained from the plasma ion measurements. The solid lines give the results for the model with mass-loading and reflective boundary conditions. The dashed lines give the results for the model with mass-loading and fixed boundary conditions.

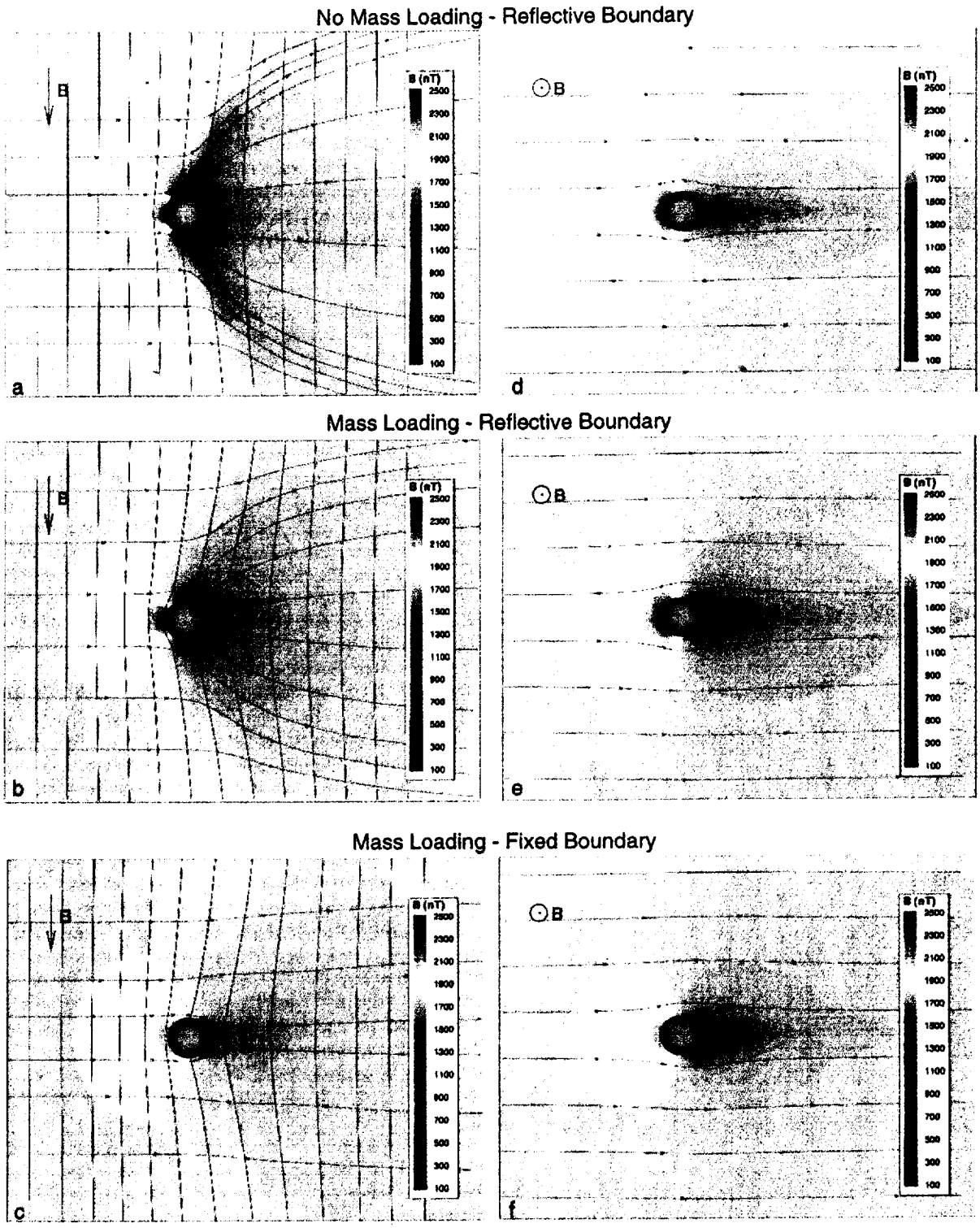

Plate 1. Magnetic field and streamlines for non-mass-loading and mass-loading flows past Io. (a)-(c) The plane aligned along the upstream magnetic field direction. The draped field lines (generally vertical lines) and velocity stream lines (generally horizontal lines with arrows) are shown. (d)-(f) The plane perpendicular to the upstream magnetic field direction. As indicated, Plates 1a and 1d correspond to the case with no mass-loading and reflective boundary conditions, Plates 1b and 1e correspond to mass loading and reflective boundary conditions, and Plates 1c and 1f correspond to the mass loading and fixed boundary conditions. The spectral color table indicates the magnitude of magnetic field. The strong influence of the Alfvén wings is apparent on the non-mass-loaded flow (Plates 1a and 1d), and is weakened with the addition of mass loading. The increased magnetic field perturbation in the wake is apparent in the mass-loaded cases. The spatial scale covers from -10 to +12 Io radii horizontally and to ±8 Io radii vertically.

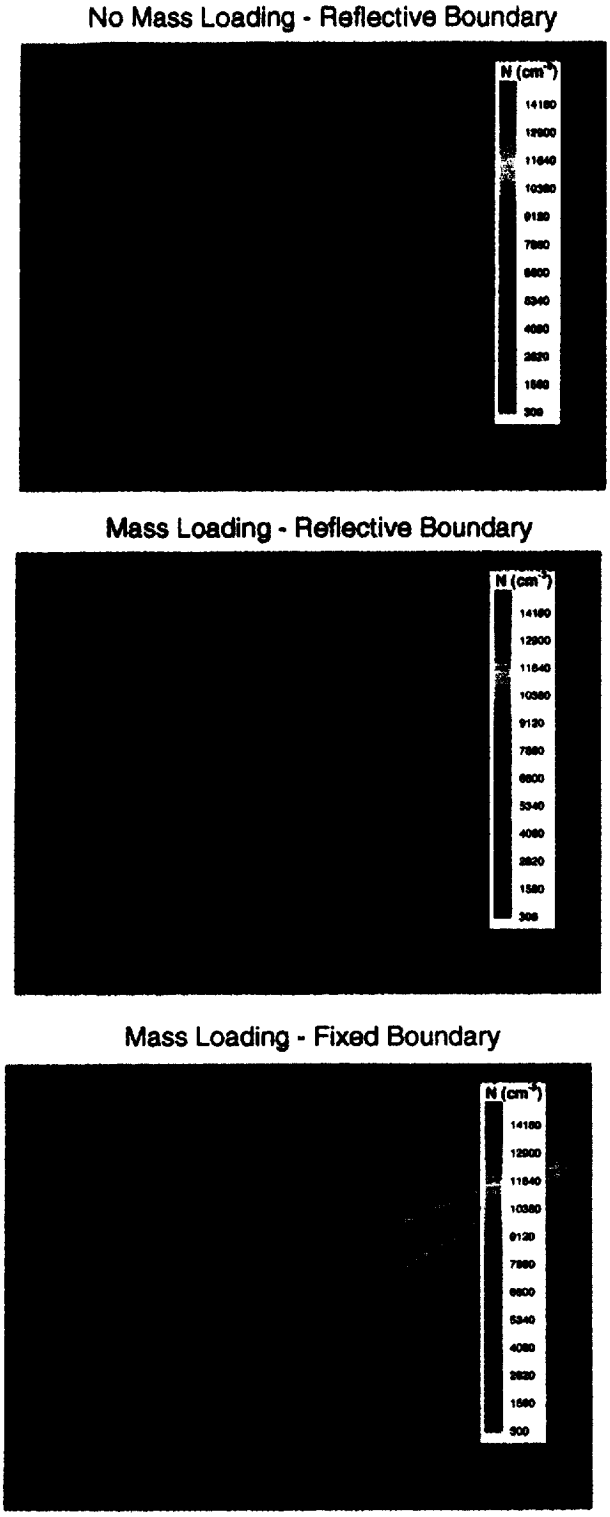

Plate 2. Plasma density for the non-mass-loading and mass-loading flows past Io. (a) The plasma density for the models with no mass-loading and reflective boundary conditions, in (b) for mass-loading and reflective boundary conditions, and in (c) for mass-loading and fixed boundary conditions. The non-mass-loading model (Plate 2a) produces a rarefied region in the wake, contrary to the Galileo particle measurements. Both mass-loading models (Plate 2b and 2c) produce a strong density peak in the wake behind Io. The symmetry line through Io covers distances from -4 to +8 Io radii.

Voyager-era estimates but may be consistent with the apparent overall larger Io atmosphere and torus activity in recent times compared with the Voyager era.

The general flow pattern in both mass-loading models is similar to the typically suggested qualitative pictures. For example, see *Schneider et al.* [1991]. Very close to Io and especially in the extended wake region the flow is very slow (a few km s^{-1}) where the effects from the locally produced ions and from charge exchange are most important. Because the Galileo trajectory is nearly in the perpendicular plane and because there is not much difference between the two models in this plane a comparison of the velocity field with the Galileo results provides little discrimination between the two alternative boundary conditions. Figure 2 shows the flow velocity vectors along the spacecraft trajectory for both mass-loading models, which give virtually identical results. The flow directions and change in the velocity magnitude in the orbit plane are quite similar to those shown in Figure 1 of *Frank et al.* [1996]. Note again, however, that Frank et al. reported asymptotic velocity magnitudes far from the wake (4 Io radii) somewhat below strict corotation (45 km s^{-1} as opposed to 56 km s^{-1}). They warned that their uncertainties were asymmetric and large enough to include strict corotation, being dependent on the details of their assumed plasma ion composition. Our model results yield corotational velocities far from Io, with somewhat supercorotational velocities (13% enhancements) in the immediate flanks of the wake near Io, about 2 Io radii from the center of the wake.

In ideal MHD the current density can be calculated as the curl of the magnetic field vector. Extracting quantities determined from components of field gradients near Io, where they are largest, is uncertain because of the presence of cut-cells (partial cubes which contain the inner boundary at one face), because of the conversion from cell-averaged parameters to node-values, and because of boundary effects. For the model runs shown here the cell structure was not optimized to obtain highly accurate currents. We can say at least qualitatively that the largest values of the current density in all three models occur near the body. As one might expect, currents associated with the Alfvén wings are the strongest in the non-mass-loading reflective boundary model and weakest for the mass-loading fixed boundary model. In the mass-loading fixed boundary model we can also estimate the integrated current from the current density near Io to be on the order of a few x 10^6 amperes. This is comparable to independently estimated values [*Khurana et al.*, 1997] for both the Galileo and Voyager epochs.

Preliminary pictures of the global shape of the local ionosphere of Io have been presented based on radio occultation measurements by *Flasar et al.* [1997] and plasma wave measurements by *Gurnett et al.* [1997]. This overall shape is dominated by the dense, stagnant, and heavily mass-loaded region indicated by the very low velocities which excludes the outer plasma torus flow, as seen in Plate 2. It is apparent then that the overall structure of Io's upper ionosphere may be largely controlled by the combination of mass loading and plasma torus flow past Io. Furthermore, the upstream-dawn and downstream-dusk ionosphere profile asymmetry seen in the Pioneer 10 radio occultation measurements [*Kliore et al.*, 1974, 1975], that are qualitatively similar to the preliminary Galileo measurement, is then most likely an upstream/downstream phenomenon rather than a

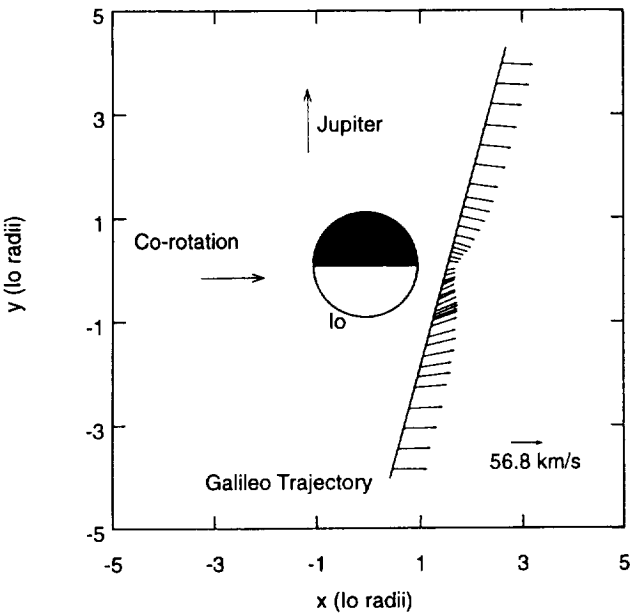

Figure 2. Velocity flow vectors along the December 1995 Galileo flyby trajectory. Shown along the projected trajectory in Io's orbit plane are the velocity vectors (direction and magnitude) from our mass-loaded MHD model calculations. The results for the fixed boundary model are shown but the reflective boundary model is virtually identical. Both the variations in direction and variation in magnitude of the velocity are quite similar to those by *Frank et al.* [1996] obtained from the Galileo plasma ion measurements. The absolute velocities from the measurements are uncertain at this time.

dawn-dusk one. This has been noted previously by *Kivelson et al.* [1979]. Preliminary Hubble Space Telescope measurements of atomic oxygen and sulfur emissions near Io [*Trauger et al.*, 1997; *Ballester et al.*, 1997] also seem to show the presence of a bright wake.

Our case of reflective boundary conditions considers the ionosphere to be a perfectly conducting and reflecting sphere at 150 km altitude above the surface, somewhat above the electron density peak [*Flasar et al.* 1997; *Kliore et al.* 1974 & 1975]. This is certainly an overestimate of even a large but finite conductivity. Our fixed boundary condition allows plasma and magnetic flux to pass, but may underestimate the effect of the underlying high ion densities (50,000 - 90,000 cm^{-3}) at the ionospheric peak near 80 km where the ions are likely more coupled with the neutral atmosphere, increasing the conductivity. In any case these two limiting cases likely bracket the true influence of a more realistic lower ionosphere/ atmosphere on the outside flow. It is interesting to note that the choice of the boundary conditions does not drastically effect the character of the direct comparison with the Galileo measurements themselves, although it does substantially change the character of the flow above and below Io in the plane parallel to the upstream magnetic field where there are as yet no Galileo data. Because of the larger deflection in the field-aligned direction for the reflective compared with the fixed boundary conditions, a higher mass-loading rate is required for the reflective case.

Note that we have already mentioned that our model with no intrinsic field, but with mass-loading and charge exchange can produce the magnetic field signature about as well as the vacuum superposition model of *Kivelson et al.* [1996b]. Assuming almost the same background field composed of a superposition of Jupiter's field and the intrinsic dipole as that of *Kivelson et al.* [1996b], *Khurana et al.* [1997] have recently presented a calculation of the magnetic field perturbation that would result from the plasma pressure as measured by Galileo PLS [*Frank et al.*, 1996]. We refer here to the broad peaks in plasma pressure (and temperature) which appear in the flanks at about 2 R_{Io} from the center of the wake. There is no corresponding density increase at this location, but it does coincide with the broad magnetic field signature. They conclude that given the validity of their assumptions only ~30% of the total field perturbation can be due to plasma effects as separate from an intrinsic magnetic field. In contrast both our models without an intrinsic magnetic field are able to account for roughly 2/3 of the total disturbance in magnetic and all of the density peak.

Although our mass-loading profile does account for the density peak, and our charge exchange profile accounts for the temperature and pressure minimum in the center of the wake they do not produce the large broad temperature and pressure peaks and the corresponding larger magnetic field disturbance in the flanks of the wake. If as *Khurana et al.* [1997] found, the enhanced plasma pressure in the flanks of the wake can account for the general breadth and depth of the magnetic field disturbance (remember this is just outside the density peak), then it is equally reasonable to conclude that if we could add a process or mechanism which would produce the enhanced temperature (and resulting pressure in absence of increased density), it should similarly also produce the correct enhanced magnetic field disturbance in our model without an intrinsic magnetic field, just as it does for their model.

Clearly then what is required is to alter our formulation to include a process which adds energy (or possibly subtracts less energy) in the flanks of the wake and/or upstream of the flanks. We consider two immediately apparent possible candidates: (1) the spatial dependence of the mass-loading and charge exchange rates, and (2) the formulation of the ion pickup process. In absence of including a detailed ion-chemical network, we adopted mass-loading and charge exchange rates which are both everywhere proportional to the measured neutral sodium radial profile of *Schneider et al.* [1991]. If the mass-loading rate and charge exchange rates are in reality not proportional to one another everywhere, it might be possible to enhance the temperature in the flanks of the wake. This increased temperature would necessarily have a corresponding increased pressure (where there is no increased density) and by the same argument as *Khurana et al.* [1997] there should also be a corresponding further decreased magnetic field. It is worth noting that our models produce somewhat super-corotational velocities enhanced by 13% just at 2 R_{Io} from the center line of the wake, exactly where the temperature is enhanced. A different velocity dependence on collision cross sections would in general be expected for the different relevant ionization and charge exchange (and knock-on) processes.

The precise forms for the ion-mass-loading and ion-neutral momentum-energy exchange (charge exchange) as functions of location around Io are in reality set by the interplay of a whole series of ion, neutral, and electron impact reactions which depend on the detailed composition of both the neutral

atmosphere and plasma. Including all the effects of this kind of detailed picture for the Io flow problems has already been done for the comet solar-wind flow problem in terms of successful comparisons with in situ spacecraft data [*Gombosi et al.*, 1996] and 2-D ground-based spectra and images for H_2O^+ [*Häberli et al.*, 1997]. In the comet problem, although much more complicated in terms of total species and reactions than for Io, the details of the neutral atmosphere structure and composition are also much better understood than for Io.

The second possibility would be to reexamine the premise behind the formulation of the pick-up process. As mentioned in the model description, the ion pick-up process adopted assumes ions are produced initially in a pick-up ring and shortly thereafter scattered into a shell distribution by wave-particle interactions. Recent Hubble Space Telescope images of the Jupiter aurora with the new STIS instrument [*Clarke et al.*, 1997] show that the footprint of Io is accompanied by a trailing footprint of the wake itself extending up to one-quarter to one-half way around Jupiter. This implies that ions picked up at Io, are still being pitch angle scattered into the loss cone for 3 to 6 hours, and still precipitating along wake-crossing flux tubes into Jupiter's ionosphere for a quarter to a half a Jupiter rotation. Those picked up very close to Io, where densities are high, would be scattered immediately. This could also explain why the models provide an excellent match to all the measurements in the densest regions. The inclusion of pickup ions remaining in ring distributions would substantially alter the formulation of the MHD equations. A multispecies model that could account for a mixed ring and shell populations is beyond our current capability. It is certainly well beyond any modeling that has yet been published. It is possible that the inclusion of this process (W. Smyth, private communication, 1997) might have desired effect on the magnetic field disturbance.

4. Summary

We have demonstrated the application of an ideal MAUS-MHD model to the interaction of Jupiter's corotating plasma torus with Io's atmosphere. The model solves the single-fluid MHD flow in 3-D on an adaptively refined mesh. Because of its numerical robustness and the ability to adapt the grid structure to the flow, the heavily mass-momentum-energy loaded flow in the supersonic and sub-Alfvénic regime relevant for the interaction of Jupiter's plasma torus has been solved without the need to introduce artificial dissipative terms.

We find that we can reproduce many of the observed structures of the plasma wake behind Io as measured by various Galileo instruments. We obtain a good quantitative match to the plasma density peak, the plasma pressure and temperature minima at the center of the wake, and the vector velocity plasma flow directions .and magnitude variations. We obtain a qualitative match to the overall pressure and temperature profiles. We reproduce the magnetic field disturbance about as well as the intrinsic dipole magnetic field model of *Kivelson et al.* [1996b]. The distant flanks of the disturbance indicate a more decreased magnetic field as well as corresponding increased plasma pressure and temperature which appear to be coincident and possible correlated. Although the responsible mechanism is not yet known, it may be due to decreased cooling in the flanks from velocity-dependent collision cross sections (which are not yet taken into account) or from the influence of pickup ions that are still in ring distributions.

Acknowledgments. This work was supported by the NASA Planetary Atmospheres Program under grant NAGW-3417, the NSF-NASA-AFOSR interagency grant NSF ATM-9318181, and by NASA HPCC CAN NCCS5-146. We thank M. Kivelson and the Galileo Magnetometer team for providing us with electronic versions of the their data and for helpful conversations regarding the interpretation of their data and our model results. We thank both referees for their critical comments which have helped us to improve this paper. Conversations with W. H. Smyth, J. Linker, J. Clarke, F. Bagenal, C. Groth, and T. Linde were also very helpful.

The Editor thanks two referees for their assistance in evaluating this paper.

References

Ballester, G. E., M. A. McGrath, D. F. Strobel, X. Zhu, P. D. Feldman, and H.W. Moos, Detection of the SO_2 atmosphere on Io with the Hubble Space Telescope, *Icarus, 111*, 2, 1994.

Ballester, G. E., J. T. Clarke, D. Rego, M. Combi, N. Larsenn, J. Ajello, D.F. Strobel, N.M. Schneider, and M. McGrath, Characteristics of Io's far-UV neutral oxygen and sulfur emissions derived from recent HST observations, *Bull. A. A. S. 28*, 1156, 1996.

Ballester, G. E., J. T. Clarke, M. Combi, D.F. Strobel, N. Larsenn, M. McGrath, M. Lenigan, J. Ajello, N.M. Schneider, and D. Rego, Io's far-ultraviolet emissions as observed with HST and IUE, *Bull. A. A. S. 29*, 980, 1997.

Belton, M. J. S., et al., Galileo's first images of Jupiter and the Galilean satellites, *Science, 274*, 377, 1996.

Bigg, E.K., Influence of the satellite Io on Jupiter's decametric emission, *Nature, 203*, 1008-1010, 1964.

Clarke, J.T., G. Ballester, J. Trauger, J. Ajello, W. Pryor, K. Tobiska, H. Waite, R. Gladstone, B. Jaffel, J. Connerney, and J.C. Gerard, HST observations of Jupiter's UV aurora during Galileo in situ measurements, *Eos Trans. AGU, 78* (46), Fall Meet. Suppl., F414, 1997.

Cloutier, P.A., R.E. Daniell, Jr., A.J. Dessler, and T.W. Hill, A cometary ionosphere model for Io, *Astrophys. Space Sci., 55*, 93, 1978.

DeZeeuw, D. L., and K.G. Powell, An Adaptively-refined Cartesian mesh solver for the Euler equations, *J. Comput. Phys., 104*, 55, 1992.

DeZeeuw, D.L., T.I. Gombosi, K.G. Powell, T.J. Linde, Multiscale modeling of the solar wind-magnetosphere-ionosphere coupling with a 3D adaptive MHD model, *Eos, Trans. AGU, 77* (46), Fall Meet. Suppl., 639, 1996.

Flasar, M., D.P. Hinson, A.J. Kliore, P.J. Schinder, J.D. Twicken, R. Woo, R. Herrera, S. Asmar, D. Chong, and P. Priest, Jupiter's Ionosphere: A review of Galileo radio-occultation measurements, *Ann. Geophys., 15* (III), 825, 1997.

Frank, L. A., W. R. Paterson, K. L. Ackerson, V. M. Vasyliunas, F. V. Coroniti, and S. J. Bolton, Plasma observations at Io with the Galileo spacecraft, *Science, 274*, 394, 1996.

Goertz, C.K., Io's interaction with the plasma torus, *J. Geophys. Res., 85*, 2949, 1980.

Goertz, C.K., D.E. Jones, B.A. Randall, E.J. Smith, and M.F. Thomsen, Evidence for open field lines in Jupiter's magneosphere, *J. Geophys. Res., 81*, 3393, 1976.

Goldreich, P., and D. Lynden-Bell, Io, A unipolar inductor, *Astrophys. J., 156*, 59-78, 1969.

Gombosi, T. I., D. L. De Zeeuw, R. M. Häberli, and K. G. Powell, Three-dimensional multiscale MHD model of comet plasma environments, *J. Geophys. Res., 101*, 15333, 1996.

Gurnett, D. A., W. S. Kurth, A. Roux, S. J. Bolton, and C. F. Kennel, Galileo plasma wave observations in the Io plasma torus and near Io, *Science, 274*, 391, 1996.

Gurnett, D.A., W. Kurth, A. Roux, S. Perraut, and T. Chust, Galileo plasma wave observations at Jupiter, *Ann. Geophys., 15* (III), 825, 1997.

Häberli, R.M., M.R. Combi, T.I. Gombosi, D.L. DeZeeuw, and K.G. Powell, Quantitative analysis of H_2O coma images using a multiscale MHD model with detailed ion chemistry, *Icarus, 130*, 373, 1997.

Hill, T.W., A.J. Dessler, and C.K. Goertz, Magnetospheric models, in *Physics of the Jovian Magnetosphere*, edited by A. J. Dessler, p. 353, Cambridge Univ. Press, New York, 1983.

Johnson, R.E., *Energetic Charged-Particle Interactions With Atmospheres and Surfaces*, Springer-Verlag, New York, 1990.

Khurana, K., M.G. Kivelson, and C.T. Russell, Interaction of Io with its torus: Does it have an internal magnetic field? *Geophys. Res. Lett., 24*, 2391, 1997.

Kivelson, M.G., J.A. Slavin, and D.J. Southwood, Magnetospheres of the Galilean satellites, *Science, 205*, 491, 1979.

Kivelson, M. G., K. K. Khurana, R. J. Walker, C. T. Russell, J. A. Linker, D. J. Southwood, and C. Polanskey, A magnetic signature at Io: Initial report from the Galileo magnetometer, *Science, 273*, 337, 1996a.

Kivelson, M. G., K. K. Khurana, R. J. Walker, J. Warnecke, C. T. Russell, J. A. Linker, D. J. Southwood, and C. Polanskey, Io's interaction with the plasma torus: Galileo magnetometer report, *Science, 274*, 296, 1996b.

Kliore, A., D.L. Cain, G. Fjeldbo, and B.L. Seidel, Preliminary results on the atmosphere of Io and Jupiter from the Pioneer 10 s-band occultation experiment, *Science, 183*, 323, 1974.

Kliore, A., G. Fjeldbo, B.L. Seidel, D.N. Sweetnam, T.T. Sesplaukis, P.M. Woiceshyn, Atmosphere of Io from Pioneer 10 radio occultation measurements, *Icarus, 24*, 407, 1975.

Kogan, M.N., On the vortices and currents in magnetofluid dynamics; *Dokl. Akad. Nauk SSSR, 139*, 58, 1961.

Lellouch, E., M. Belton, I. De Pater, G. Paubert, S. Gulkis, and T. Encrenaz, The structure, stability, and global distribution of Io's atmosphere, *Icarus, 98*, 271, 1992.

Linker, J.A., M.G. Kivelson, and R.J. Walker, An MHD simulation of plasma flow past Io: Alfvén and slow mode perturbations, *Geophys. Res. Lett., 15*, 1311, 1988.

Linker, J.A., M.G. Kivelson, and R.J. Walker, The effect of mass loading on the temperature of a flowing plasma, *Geophys. Res. Lett., 16*, 763, 1989.

Linker, J.A., M.G. Kivelson, and R.J. Walker, A Three-dimensional MHD simulation of plasma flow past Io, *J. Geophys. Res., 96*, 21037, 1991.

McGrath, M.A. and R.E. Johnson, Magnetospheric plasma sputtering of Io's atmosphere, *Icarus, 69*, 519, 1987.

McGrath, M.A., and R.E. Johnson, Charge exchange cross sections for the Io plasma torus, *J. Geophys. Res., 94*, 2677, 1989.

Moreno, M. A., G. Schubery, J. Baumgardner, M. G. Kivelson, and D. A. Paige, Io's volcanic and sublimation atmospheres, *Icarus , 93*, 63, 1991.

Neubauer, F.M., Nonlinear standing Aflvén wave current system at Io: Theory, *J. Geophys. Res., 85*, 1171, 1980.

Pospieszalska, M. K., and R. E. Johnson, Monte Carlo calculations of plasma ion-induced sputtering of an atmosphere: SO_2 ejected from Io, *J. Geophys. Res. 101*, 7565, 1996.

Powell, K.G. An approximate Riemann solver for magnetohydrodynamics (that works in more than one dimension), *ICASE Rep. 94-24*, 1994.

Powell, K. G., P. L. Roe, R. S. Myong, T. I. Gombosi, and D. L. De Zeeuw, An upwind scheme for magnetohydrodynamics, *AIAA Pap. 95-1704-CP*, 1995.

Russell, C.T., F. Bagenal, A.F. Cheng, W-H. Ip, A. Roux, W.H. Smyth, S.J. Bolton, and C.A. Polanskey, Io's interaction with the Jovian magnetosphere, *Eos, Trans. AGU, 78*, (9), 95, 1997.

Schneider, N.M., W.H. Smyth, and M.A. McGrath, Io's atmosphere and neutral clouds, in Time-variable phenomena in the Jovian system, *Proceedings of the Workshop on Time-variable Phenomena in the Jovian system*, NASA Spec. Publ., *NASA SP- 494*, 75-99, 1989.

Schneider, N.M., D.M. Hunten, W.K. Wells, A.B. Schultz, and U. Fink, The structure of Io's corona, *Astrophys. J., 368*, 298, 1991.

Shemansky, D.E., Mass-loading and diffusion-loss rates of the Io plasma torus, *Astrophys. J., 242*, 1266, 1980.

Sieveka, E. M., and R. E. Johnson, Nonisotropic coronal atmosphere on Io, *J. Geophys. Res., 90*, 5327, 1985.

Smyth, W.H., Neutral cloud distribution in the Jovian system, *Adv. Space Res.*, 12(8), 8337, 1992.

Smyth, W. H., and M. R. Combi, Io's sodium corona and spatially extended cloud: A consistent flux speed distribution, *Icarus, 126*, 58-77, 1997.

Smyth, W.H., and D. E. Shemansky, Escape and ionization of atomic oxygen from Io, *Astrophys. J., 271*, 865, 1983.

Southwood, D.J., M.G. Kivelson, R.J. Walker, and J.A. Slavin, Io and its plasma environment, *J. Geophys. Res., 85*, 5959, 1980.

Strobel, D. F., X. Zhu, and M.E. Summers, On the vertical thermal structure of Io's atmosphere, *Icarus, 11*,1 18, 1994.

Trauger, J.T., K.R. Stapelfeldt, G.E. Ballester, J.T. Clarke, and WFPC2 Science Team, HST observations of [OI] emissions from Io in eclipse, *Bull. A. A. S., 29*, 1002, 1997.

van Leer, B., Towards the ultimate conservative difference scheme, V, A second-order sequel to Godunov's method, *J. Comput. Phys., 32*, 101, 1979.

Williams, D. J., B. H. Mauk, R. E. McEntire, E. C. Roelof, T. P. Armstrong, B. Wilken, J. G. Roederer, S. M. Krimigis, T. A. Fritz, and L. J. Lanzerotti, Electron beams and ion composition measured at Io and in its torus, *Science, 274*, 401, 1996.

Wolf-Gladrow, D.A., F.M. Neubauer, and M. Lussem, Io's interaction with the plasma torus: A self-consistent model, *J. Geophys. Res., 92*, 9949, 1987.

Wong, M. C., and R.E. Johnson, The effect of Plasma heating on sublimation-driven flow in Io's atmosphere, *Icarus, 115*, 109, 1995.

M. R. Combi, D. L. De Zeeuw, T. I. Gombosi, and K. Kabin, Space Physics Research Laboratory, University of Michigan, 2455 Hayward Street, Ann Arbor, MI 48109-2143. (e-mail: mcombi@umich.edu)

K. G. Powell, Department of Aerospace Engineering, University of Michigan, Ann Arbor, MI 48109-2118.

(Received May 16, 1997; revised December 29, 1997;
accepted December 31, 1997.)

UNIVERSITY OF MICHIGAN
COLLEGE OF ENGINEERING
ATMOSPHERIC, OCEANIC AND SPACE SCIENCES

SPACE RESEARCH BUILDING
2455 HAYWARD
ANN ARBOR, MICHIGAN 48109-2143
TELEPHONE: 734 764-3335 FAX: 734 764-4585

6 October 1999

Reta Beebe
NASA Headquarters, Code SR
Washington, DC 20546

Subject: Final Technical Report Grant No. NAG5-1687

Dear Ms Beebe:

On behalf of the project director, Michael Combi, and in compliance with the requirements of the grant NAG5-1687 entitled "Studies for the Loss of Atomic and Molecular Species From IO", I am forwarding the enclosed fianl technical report.

If you have any questions or need additional information please contact Michael Combi at (734)764-7226.

Sincerely,

Cheri Hovater
Administrative Assistant

ch

encls.

cc: NASA/ CASI
Lisa Foster
ONR, Chicago w/o incls.
N. Gerl w/o encls.
file 030724